Phase-field modeling of crack propagation in heterogeneous materials with multiple crack order parameters

Lukas Schöller[a,*], Daniel Schneider[a,b], Christoph Herrmann[a], Andreas Prahs[a], Britta Nestler[a,b]

[a] *Institute for Applied Materials (IAM-MMS), Karlsruhe Institute of Technology (KIT), Strasse am Forum 7, 76131 Karlsruhe, Germany*
[b] *Institute of Digital Materials Science (IDM), Karlsruhe University of Applied Sciences, Moltkestrasse 30, 76133 Karlsruhe, Germany*

Abstract

The phase-field method is widely established for modeling crack propagation in material science. It shows good agreement with analytical solutions and is able to describe a complex fracture behavior. Nevertheless, the models are mostly introduced for homogeneous systems, and there are only a few approaches for heterogeneous systems. So models, that are able to describe the crack propagation in such systems, are highly desirable. Based on a classic crack propagation phase-field approach, existing models are discussed, and a new model is derived. The first model, which is based on an already existing approach, uses homogenized properties and a single-crack order parameter, while the second model, a new approach, introduces multiple crack order parameters, each of which only tracks the damage of a corresponding phase. Furthermore, the issues of the single-crack order parameter model are demonstrated, such as the ability to reproduce the quantitative surface energies for an interfacial crack and the non-physical behavior of a crack propagating along a sloped material interface. In contrast, the novel multi-crack order parameter model prevents distortions for an interfacial crack and propagates along the interface in a more physical manner. In comparison with an analytical solution, based on linear elastic fracture mechanics, the novel model shows a good agreement, even for strongly sloped interfaces, where the single-crack order parameter model fails to reproduce the analytical solution. In a subsequent application to fiber-reinforced polymers, the new model has proven to be able to predict fractures in complex systems, including crack nucleation, branching, and merging. Finally, the applicability to a 3D system is illustrated.

Keywords: Fracture mechanics; Crack propagation; Multi-phasefield; Heterogeneous materials; Fiber reinforced polymers

1. Introduction

Understanding failure and fracture behavior is a challenge in modern engineering and materials science, especially when considering the growing number of materials with a complex morphology and heterogeneous material properties, such as fiber-reinforced polymers (FRP). Predicting the resistance to failure and the complex crack propagation paths of such materials will improve the ability to determine effective load capacities and to develop

* Corresponding author.
E-mail address: lukas.schoeller@kit.edu (L. Schöller).

efficient, safe, and predictable products. Linear Elastic Fracture Mechanics (LEFM) has proven to be capable of describing crack propagation in homogeneous materials in 2D [1,2]. An extension to heterogeneous materials is possible [3,4], but a general approach which describes complex heterogeneous materials in 3D seems difficult and not feasible. An alternative approach is cohesive zone modeling (CZM), introduced by Barenblatt [5] and Dugdale [6], which can be embedded in the finite element method (FEM), using cohesive finite elements. An overview of CZM can be found in Elices et al. [7]. Since these models demand for conforming meshes, more advanced crack paths require cumbersome remeshing methods. In comparison, the generalized/extended finite element method (GFEM/XFEM) enriches the solution space of the FEM to handle discontinuous functions [8]. This eliminates the need for conforming meshes and remeshing. However, both CZM and GFEM/XFEM are limited to describe complex crack propagation behavior, including nucleation, branching, or the interaction between cracks. In a domain with sharp interfaces, different regions, e.g., phases or destroyed and unbroken material, occurring in the case of fracture, are distinctly separated, cf., e.g., Prahs and Böhlke [9], in the context of interface conditions on a sharp interface. This requires explicit tracking of the interface, which has proven impractical. An alternative approach to fracture utilizes the phase-field method (PFM), introducing order parameters to allow a smooth transition between various regions. This results in continuous order parameter fields, often referred as phase fields, and allows an implicit tracking of the interface on nonconforming meshes, and thus an efficient numerical treatment of singularities, such as grain boundaries or cracks. Thus, the PFM is widely established to describe the evolution of microstructures, such as solidification or solid–solid phase transitions, considering different types of physical aspects, e.g., thermodynamics, chemistry, or mechanics [10–14]. Phase-field approaches to brittle fracture have been developed in both the physical [15–17] and the mechanic community [18–20]. The latter is based on Griffith's theory [21] and the variational formulation of Francfort and Marigo [22] and Francfort and Bourdin et al. [23]. Other more advanced applications, for example, deal with plasticity [24–27] or multiphysics [28–31]. For most of these models, the material is considered homogeneous. This is a reasonable assumption on macroscopic length scales. Often, however, failure mechanisms occur at smaller length scales, where many materials are heterogeneous. Therefore, models that are able to describe fracture of heterogeneous systems are highly desirable.

Most phase-field models describing crack propagation in such systems introduce a varying crack surface energy. This is achieved either by anisotropy [32,33] or interpolation of the surface energy [34,35]. Schneider et al. [36] proposed a model that extends the multi-phase field model of Nestler et al. [37], so as to describe crack propagation in polycrystalline systems. The model takes into account damage due to a phase transition to a common crack phase. This concept has also been extended to anisotropy [38] and plasticity [39]. A common approach to consider an interfacial fracture toughness is to lower the crack resistance in the interfacial region. Hansen-Dörr et al. [40,41], for instance, model a locally varying value based on a virtual phase transition. To account for interfacial effects, CZM have also been introduced into phase-field crack propagation models [42–45]. Although these models can describe complex crack propagation in heterogeneous materials, including interfacial effects, and agree with the LEFM and experiments, they can lead to non-physical behavior as discussed by Henry [46].

The objective of the paper is to introduce a novel multi-crack order parameter (MCOP) phase-field model for fracture which is able to overcome issues of the established single-crack order parameter (SCOP) approaches for modeling crack propagation in heterogeneous systems based on the phase-field method. Therefore, some issues of the SCOP model are illustrated in simple 1D and 2D simulation setups and several advantages of the novel model are demonstrated. This paper is structured as follows: Section 2 introduces the phase-field crack propagation models for the homogeneous and heterogeneous case and the corresponding governing equations are derived, while Section 3 gives remarks on the numerical implementation. Followed by a discussion of the numerical results in Section 4 of both heterogeneous models in 1D, two limiting cases for a binary interface in 2D, including a comparison to analytical solution from the LEFM, and an application to FRP in 2D and 3D are presented.

2. Phase-field crack propagation models

For a material body $\Omega \in \mathbb{R}^n$ $n \in \{1, 2, 3\}$, in an Euclidean space, the displacement vector $\boldsymbol{u}$ relates the position vector of a material point regarding the reference and the current configuration. The boundary of the body $\partial\Omega \in \mathbb{R}^{n-1}$ consists of a subset $\partial\Omega_{\mathrm{D}}$, on which a Dirichlet boundary condition is applied, by prescribing the displacement vector $\boldsymbol{u} = \overline{\boldsymbol{u}}$, while a Neumann boundary condition is imposed on $\partial\Omega_{\mathrm{N}}$, for which the stress vector $\boldsymbol{t} = \overline{\boldsymbol{t}}$ is specified. For both boundaries, $\partial\Omega_{\mathrm{D}} \cup \partial\Omega_{\mathrm{N}} = \partial\Omega$ and $\partial\Omega_{\mathrm{D}} \cap \partial\Omega_{\mathrm{N}} = \emptyset$ must apply. In addition, the body contains a sharp crack surface S_{c}.

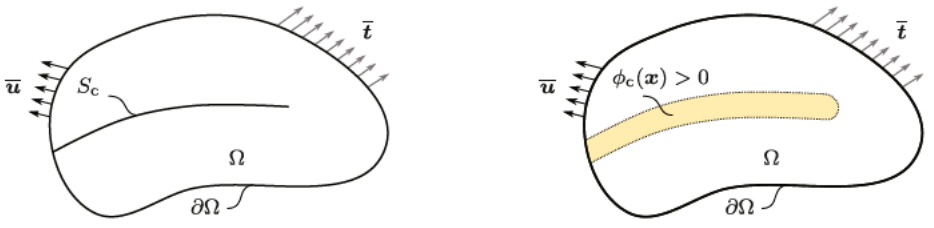

Fig. 1. Schematic homogeneous domain with a sharp crack interface (a) and a diffuse crack interface in yellow (b). (For interpretation of the references to color in this figure legend, the reader is referred to the web version of this article.)

2.1. Classical homogeneous model

Free energy functional. For a homogeneous domain containing a sharp crack, cf. Fig. 1(a), the free energy functional is proposed by

$$\mathcal{F}[\boldsymbol{u}] = \int_{\Omega} f_{\mathrm{el}}(\boldsymbol{u})\,\mathrm{d}v + \int_{S_c} G_c\,\mathrm{d}a, \tag{1}$$

with a strain energy density $f_{\mathrm{el}}(\boldsymbol{u})$ and a critical energy release rate G_c, which describes the surface energy density γ for the sharp crack surface by $G_c = 2\gamma$. The introduction of the crack order parameter $\phi_c \in [0, 1]$ enables a smooth transition of the material state. For $\phi_c = 1$, the material is fully broken, for $\phi_c = 0$, it remains undamaged. Following Kuhn and Müller [19], this allows the free energy (1) to be rewritten by a volume integral

$$\mathcal{F}[\boldsymbol{u}, \phi_c, \nabla\phi_c] = \int_{\Omega} \underbrace{h(\phi_c)\, f_{\mathrm{el}}(\boldsymbol{u}) + \frac{1}{2} G_c \left(\epsilon_c\, |\nabla\phi_c|^2 + \frac{1}{\epsilon_c}\phi_c^{\,2} \right)}_{f(\boldsymbol{u}, \phi_c, \nabla\phi_c)} \mathrm{d}v, \tag{2}$$

cf. Fig. 1(b). The strain energy density is degraded by the function $h(\phi_c) = (1 - \phi_c)^2$. For a general discussion of degradation functions, the reader is referred to Kuhn et al. [47]. The energy of the crack is parametrized by a $\phi_c{}^2$ and a gradient term with the spatial gradient $\nabla\phi_c = \mathrm{grad}(\phi_c)$ and its norm $|\nabla\phi_c| = \sqrt{\nabla\phi_c \cdot \nabla\phi_c}$. In addition, the length parameter ϵ_c defines the width of the diffuse interface.

Strain energy density. The elastic term of the free energy functional (2) is modeled by an elastic potential, assuming small deformations. Thus, the strain energy density reads

$$f_{\mathrm{el}}(\boldsymbol{u}) = \frac{1}{2}\boldsymbol{\sigma} \cdot \boldsymbol{\varepsilon}, \tag{3}$$

with the strain tensor $\boldsymbol{\varepsilon} = \mathrm{sym}(\mathrm{grad}(\boldsymbol{u}))$, where $\mathrm{sym}(\cdot)$ denotes the symmetric part of a second order tensor. In addition, Hooke's law

$$\boldsymbol{\sigma} = \mathbb{C}\,[\boldsymbol{\varepsilon}]\,, \tag{4}$$

is assumed, with the symmetric Cauchy stress tensor $\boldsymbol{\sigma}$, and the 4^{th} order stiffness tensor $\mathbb{C}$. Moreover, body forces are neglected and a quasi-static behavior is considered, subsequently. For an isotropic case, this constitutive equation simplifies to $\boldsymbol{\sigma} = \lambda \mathrm{tr}(\boldsymbol{\varepsilon})\,\mathbf{1} + 2\mu\boldsymbol{\varepsilon}$, with the Lamé parameters λ and μ, the second-order identity tensor $\mathbf{1}$, and the trace operator $\mathrm{tr}(\cdot)$. The Lamé parameters can also be expressed by Young's modulus E and Poisson's ratio ν, using

$$\lambda = \frac{E\nu}{(1+\nu)\,(1-2\nu)}, \qquad \mu = \frac{E}{2\,(1+\nu)}. \tag{5}$$

As cracks typically do not evolve under compression loads, several approaches exist to split the strain energy density into a tension and compression part. By only degrading the tension part, this results in a more physical crack propagation behavior. Early tension–compression splits were introduced by Amor et al. [48], Miehe et al. [49] and Henry and Levine [17]. More recent variants were proposed by Ambati et al. [25], Strobl and Seelig [50], and Storm

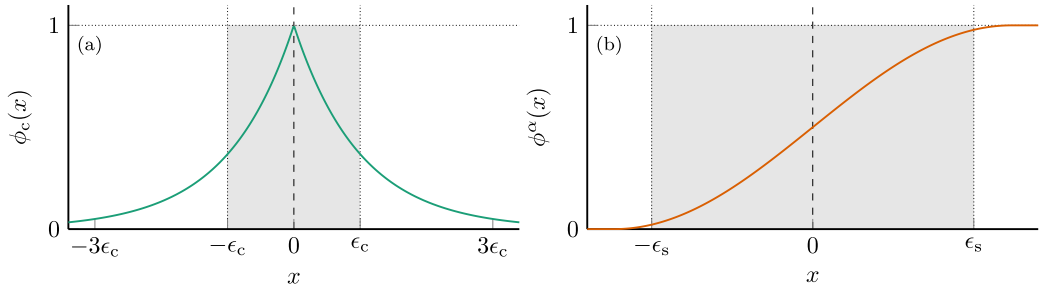

Fig. 2. Analytical order parameter profile for crack (a) and solid (b), for a corresponding sharp crack and a solid–solid interface at $x = 0$, respectively.

et al. [51]. Despite their significance, none of these variants is considered here, in order to reduce the complexity of the proposed model. However, an extension to most of the established tension–compression splits could be applied straightforwardly. Applying Eq. (3) and (4) to the functional (2), yields

$$\mathcal{F}[\boldsymbol{u}, \phi_c, \nabla\phi_c] = \int_\Omega \frac{1}{2} h(\phi_c)(\mathbb{C}\,[\boldsymbol{\varepsilon}]) \cdot \boldsymbol{\varepsilon} + \frac{1}{2} G_c \left(\epsilon_c \, |\nabla\phi_c|^2 + \frac{1}{\epsilon_c} {\phi_c}^2 \right) \mathrm{d}v. \tag{6}$$

Balance of linear momentum. Following the approach of Kuhn et al. [19], the minimization of the free energy functional (6), with respect to the displacement yields the balance of linear momentum

$$\mathrm{div}(h(\phi_c)\boldsymbol{\sigma}) = \boldsymbol{0}. \tag{7}$$

Evolution equation. The evolution equation of the order parameter ϕ_c can be described by an Allen–Cahn equation [52]

$$\epsilon_c \dot{\phi}_c = -M \frac{\delta \mathcal{F}}{\delta \phi_c} = -M \left(\frac{\partial f(\boldsymbol{u}, \phi_c, \nabla\phi_c)}{\partial \phi_c} - \mathrm{div}\left(\frac{\partial f(\boldsymbol{u}, \phi_c, \nabla\phi_c)}{\partial \nabla\phi_c} \right) \right), \tag{8}$$

with a mobility parameter $M \geq 0$, $\nabla\phi_c \cdot \boldsymbol{n} = 0$ on $\partial\Omega$ and the outer normal vector $\boldsymbol{n}$ on the boundary.

Analytical crack profile. For a one-dimensional stationary crack without mechanical loads, and thus with vanishing mechanical driving force, the evolution equation according to (8) is able to reproduce the correct surface energies of a sharp interface and lead to the analytical profile [20]

$$\phi_c(x) = \exp\left(-\frac{|x|}{\epsilon_c} \right), \tag{9}$$

which is displayed in Fig. 2a.

Irreversibility condition. Various approaches for the realization of an irreversibility condition for the evolution equation are listed in the literature: Bourdin et al. [18] used a Dirichlet boundary condition. In contrast, Miehe et al. [20] introduced a strain history function to realize the irreversibility of crack order parameter. More recent approaches use the augmented Lagrangian method [53], a primal–dual-active set [54], a complementarity system [55], or the interior point method [56]. The model introduced above reproduces the correct sharp interface energy in the case of the analytical profile (9). Since mechanical loads are considered here, the strain energy density contributes to the evolution equation of the order parameter (8). This leads to a distorted profile, if crack healing is prevented completely, and therefore to an error in the represented energy, if the applied load is removed completely. As the objective of this work is to investigate the possibility of different models to reproduce the sharp interface energies, the irreversibility is realized by a Dirichlet boundary condition, where the evolution equation is not restricted in general, but all fully damaged points remain damaged, using a boundary condition $\phi_c = 1$, where a point is assumed to be fully damaged by $\phi_c \geq 0.99$ using a numerical threshold. This improves the numerical behavior and has a negligible effect on the results. Nevertheless, the models presented in the present work could also be realized with other approaches to the irreversibility condition, which are listed above.

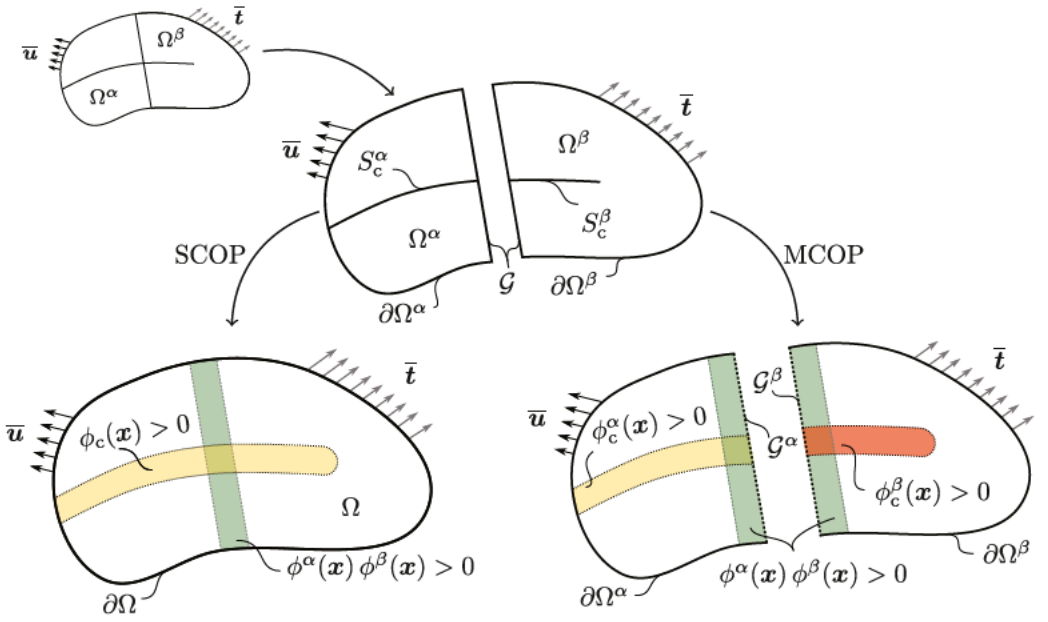

Fig. 3. Schematic heterogeneous domain for the SCOP and MCOP models: The initial domain is schematically drawn on the top left. The subdomains are visualized separately in the center, with a sharp crack interface. In the lower left, the SCOP model is shown with its diffuse crack interfaces in yellow, whereas in the lower right, the MCOP model is displayed with several diffuse crack interfaces in the subdomains Ω^α and Ω^β in red and yellow. The diffuse solid interface $\phi^\alpha(\boldsymbol{x})\phi^\beta(\boldsymbol{x})$ is indicated in green. (For interpretation of the references to color in this figure legend, the reader is referred to the web version of this article.)

2.2. Heterogeneous single-crack order parameter (SCOP) model

Solid order parameters. To distinguish different regions of a heterogeneous body, the order parameters $\phi^\alpha \in [0, 1]$, $\forall \alpha = 1, \dots, N$ are introduced for N different regions, which can be arranged in the tuple

$$\boldsymbol{\phi} = \left\{\phi^1, \phi^2, \dots, \phi^N\right\}. \tag{10}$$

A bulk region of phase α is represented by $\phi^\alpha = 1$, while a diffuse interface is represented by $0 < \phi^\alpha < 1$. As the order parameters can be interpreted as the volume fraction of the corresponding regions, the condition

$$\sum_{\alpha=1}^{N} \phi^\alpha = 1 \tag{11}$$

has to be fulfilled. By extending the free energy functional (1) with interfacial terms between the regions a multi-phase field model can be formulated, as proposed by Nestler et al. [37]. Using a double obstacle phase-field potential results in an analytical one-dimensional profile for a binary interface:

$$\phi^\alpha(x) = \frac{1}{2}\left(1 + \sin\left(\frac{\pi}{l_s}x\right)\right), \qquad -\frac{l_s}{2} \le x \le \frac{l_s}{2}, \tag{12}$$

as shown by Steinbach et al. [57], which is presented in Fig. 2b. It is characterized by the interface width l_s or, analogous to the crack profile, by a length parameter $\epsilon_s = 4/\pi^2 l_s$. Since no changes of ϕ^α are examined in this work, an extension of the free energy and a derivation of a classical multi-phase field is omitted. Instead, the analytical profile (12) is utilized to parametrize the domain, resulting in diffuse and smooth volumetric interfaces, cf. Fig. 3.

Free energy functional. To account for heterogeneous materials, the domain Ω can be decomposed into subdomains Ω^α with constant material properties, cf. Fig. 3. Thus, the energy functional for sharp interfaces follows by

$$\mathcal{F}[\boldsymbol{u}] = \sum_{\alpha}^{N} \int_{\Omega^\alpha} f_{\mathrm{el}}^{\alpha}(\boldsymbol{u})\,\mathrm{d}v + \sum_{\alpha}^{N} \int_{S_{\mathrm{c}}^{\alpha}} G_{\mathrm{c}}^{\alpha}\,\mathrm{d}a. \tag{13}$$

In the context of the SCOP model, and thus, in contrast to the functional (1), the strain energy densities f_{el}^{α} as well as the critical energy release rates G_{c}^{α} are phase-specific, denoted by the phase index α. The energy of each subdomain is given by an integral of energy densities over Ω^α, which can be parametrized using an indicator function and expanded to Ω. Subsequently, the order parameters of the solid phase field can be used as a smooth approximation to the indicator function [58,59]. This leads to a linear interpolation of the energy densities with the solid order parameters $\boldsymbol{\phi}$, cf. for example Nestler et al. [37], yielding

$$\mathcal{F}[\boldsymbol{u}] = \int_{\Omega} \sum_{\alpha}^{N} \phi^{\alpha} f_{\mathrm{el}}^{\alpha}(\boldsymbol{u})\,\mathrm{d}v + \int_{S_{\mathrm{c}}} \sum_{\alpha}^{N} \phi^{\alpha} G_{\mathrm{c}}^{\alpha}\,\mathrm{d}a. \tag{14}$$

As for the classic homogeneous model, a crack order parameter ϕ_{c} is introduced to describe the damage of the domain smoothly, and the free energy of a heterogeneous body is given by

$$\mathcal{F}[\boldsymbol{u}, \phi_{\mathrm{c}}, \nabla\phi_{\mathrm{c}}] = \int_{\Omega} h(\phi_{\mathrm{c}}) \sum_{\alpha}^{N} \phi^{\alpha} f_{\mathrm{el}}^{\alpha} + \frac{1}{2} \sum_{\alpha}^{N} \phi^{\alpha} G_{\mathrm{c}}^{\alpha} \left(\epsilon_{\mathrm{c}} \left|\nabla\phi_{\mathrm{c}}\right|^2 + \frac{1}{\epsilon_{\mathrm{c}}} {\phi_{\mathrm{c}}}^2 \right) \mathrm{d}v, \tag{15}$$

$$f_{\mathrm{el}}^{\alpha} = \frac{1}{2} \boldsymbol{\sigma}^{\alpha} \cdot \boldsymbol{\varepsilon}^{\alpha}, \qquad \boldsymbol{\sigma}^{\alpha} = \mathbb{C}^{\alpha} \left[\boldsymbol{\varepsilon}^{\alpha}\right]. \tag{16}$$

In general, the phase-inherent stresses and strains are unknown. To determine an overall material behavior, further assumptions have to be made. This is widely investigated in the context of phase-field modeling [60–64]. Recently, Prajapati et al. [38] introduced a model that applies the homogenization scheme proposed by Schneider et al. [63] in the context of a phase-field fracture model. Nevertheless, for simplicity, a Voigt–Taylor homogenization scheme is used in this work, assuming equal strains in each phase

$$\boldsymbol{\varepsilon}^{\alpha} = \boldsymbol{\varepsilon} \;\forall \alpha = 1, \ldots, N, \tag{17}$$

acknowledging the limited capabilities of this scheme [13,60]. By applying (17) and (16) to the functional (15) this yields

$$\mathcal{F}[\boldsymbol{u}, \phi_{\mathrm{c}}, \nabla\phi_{\mathrm{c}}] = \int_{\Omega} \frac{1}{2} h(\phi_{\mathrm{c}}) \sum_{\alpha}^{N} \phi^{\alpha} (\mathbb{C}^{\alpha}\left[\boldsymbol{\varepsilon}\right]) \cdot \boldsymbol{\varepsilon} + \frac{1}{2} \sum_{\alpha}^{N} \phi^{\alpha} G_{\mathrm{c}}^{\alpha} \left(\epsilon_{\mathrm{c}} \left|\nabla\phi_{\mathrm{c}}\right|^2 + \frac{1}{\epsilon_{\mathrm{c}}} {\phi_{\mathrm{c}}}^2 \right) \mathrm{d}v. \tag{18}$$

Note that the procedure to obtain the evolution equations of the crack order parameter and the balance of linear momentum is the same as for the classical phase-field crack propagation model in Section 2.1, but now including interpolations of the phase-specific stiffnesses and critical energy release rates with the order parameters ϕ^{α}.

2.3. Heterogeneous multi-crack order parameter (MCOP) model

Order parameters. As in the previous section, a tuple of order parameters,

$$\boldsymbol{\phi} = \left\{\phi^1, \phi^2, \ldots, \phi^N\right\}, \qquad \sum_{\alpha=1}^{N} \phi^{\alpha} = 1, \tag{19}$$

is introduced to parametrize different regions of a heterogeneous body. In addition, a tuple consisting of separate crack order parameters $\phi_{\mathrm{c}}^{\alpha} \in [0, 1]$, for each solid phase,

$$\boldsymbol{\phi}_{\mathrm{c}} = \left\{\phi_{\mathrm{c}}^1, \phi_{\mathrm{c}}^2, \ldots, \phi_{\mathrm{c}}^N\right\}, \tag{20}$$

is introduced. Each crack order parameter $\phi_{\mathrm{c}}^{\alpha}$ tracks the damage of the corresponding solid region α. For $\phi_{\mathrm{c}}^{\alpha} = 1$, for instance, the complete volume fraction ϕ^{α} is damaged, while other solid regions are not affected by $\phi_{\mathrm{c}}^{\alpha}$, cf. Fig. 3.

Free energy functional. The MCOP model combines the functional given by Eq. (14), used as the basis for the SCOP model, with the individual degradation of the strain energy densities f_{el}^{α} by means of multiple crack order parameters according to Eq. (20). In addition, the critical energy release rates G_{c}^{α} are also parametrized by the individual crack order parameters. This results in the free energy functional

$$\mathcal{F}\left[\boldsymbol{u}, \boldsymbol{\phi}_{\mathrm{c}}, \nabla\boldsymbol{\phi}_{\mathrm{c}}\right] = \int_{\Omega} \sum_{\alpha}^{N} \phi^{\alpha} h\left(\phi_{\mathrm{c}}^{\alpha}\right) f_{\mathrm{el}}^{\alpha} + \frac{1}{2} \sum_{\alpha}^{N} \phi^{\alpha} G_{\mathrm{c}}^{\alpha} \left(\epsilon_{\mathrm{c}} \left|\nabla\phi_{\mathrm{c}}^{\alpha}\right|^{2} + \frac{1}{\epsilon_{\mathrm{c}}} \left(\phi_{\mathrm{c}}^{\alpha}\right)^{2} \right) \mathrm{d}v, \tag{21}$$

with $\nabla\boldsymbol{\phi}_{\mathrm{c}} = \left\{\nabla\phi_{\mathrm{c}}^{1}, \nabla\phi_{\mathrm{c}}^{2}, \ldots, \nabla\phi_{\mathrm{c}}^{N}\right\}$. The free energy functional for each subdomain Ω^{α} can be identified by

$$\begin{aligned} \mathcal{F}^{\alpha}\left[\boldsymbol{u}, \phi_{\mathrm{c}}^{\alpha}, \nabla\phi_{\mathrm{c}}^{\alpha}\right] &= \int_{\Omega} \phi^{\alpha} f^{\alpha}\left(\boldsymbol{u}, \phi_{\mathrm{c}}^{\alpha}, \nabla\phi_{\mathrm{c}}^{\alpha}\right) \mathrm{d}v \\ &= \int_{\Omega^{\alpha}} \underbrace{h\left(\phi_{\mathrm{c}}^{\alpha}\right) f_{\mathrm{el}}^{\alpha} + \frac{1}{2} G_{\mathrm{c}}^{\alpha} \left(\epsilon_{\mathrm{c}} \left|\nabla\phi_{\mathrm{c}}^{\alpha}\right|^{2} + \frac{1}{\epsilon_{\mathrm{c}}} \left(\phi_{\mathrm{c}}^{\alpha}\right)^{2} \right)}_{f^{\alpha}\left(\boldsymbol{u}, \phi_{\mathrm{c}}^{\alpha}, \nabla\phi_{\mathrm{c}}^{\alpha}\right)} \mathrm{d}v. \end{aligned} \tag{22}$$

With Eq. (16) and, as in the previous model, the assumption of the Voigt–Taylor scheme (17), the functional for the whole domain and each subdomain is obtained by

$$\mathcal{F}^{\alpha}\left[\boldsymbol{u}, \phi_{\mathrm{c}}^{\alpha}, \nabla\phi_{\mathrm{c}}^{\alpha}\right] = \int_{\Omega^{\alpha}} \frac{1}{2} h\left(\phi_{\mathrm{c}}^{\alpha}\right) (\mathbb{C}^{\alpha}\left[\boldsymbol{\varepsilon}\right]) \cdot \boldsymbol{\varepsilon} + \frac{1}{2} G_{\mathrm{c}}^{\alpha} \left(\epsilon_{\mathrm{c}} \left|\nabla\phi_{\mathrm{c}}^{\alpha}\right|^{2} + \frac{1}{\epsilon_{\mathrm{c}}} \left(\phi_{\mathrm{c}}^{\alpha}\right)^{2} \right) \mathrm{d}v, \tag{23}$$

$$\mathcal{F}\left[\boldsymbol{u}, \boldsymbol{\phi}_{\mathrm{c}}, \nabla\boldsymbol{\phi}_{\mathrm{c}}\right] = \int_{\Omega} \frac{1}{2} \sum_{\alpha=1}^{N} \phi^{\alpha} h\left(\phi_{\mathrm{c}}^{\alpha}\right) (\mathbb{C}^{\alpha}\left[\boldsymbol{\varepsilon}\right]) \cdot \boldsymbol{\varepsilon} + \frac{1}{2} \sum_{\alpha=1}^{N} \phi^{\alpha} G_{\mathrm{c}}^{\alpha} \left(\epsilon_{\mathrm{c}} \left|\nabla\phi_{\mathrm{c}}^{\alpha}\right|^{2} + \frac{1}{\epsilon_{\mathrm{c}}} \left(\phi_{\mathrm{c}}^{\alpha}\right)^{2} \right) \mathrm{d}v. \tag{24}$$

As in the previous models, minimizing the latter functional with respect to the displacements yields the balance of linear momentum and is therefore omitted here.

Evolution equation. For each crack order parameter an Allen–Cahn equation,

$$\epsilon_{\mathrm{c}} \dot{\phi}_{\mathrm{c}}^{\alpha} = -M^{\alpha} \frac{\delta\mathcal{F}^{\alpha}}{\delta\phi_{\mathrm{c}}^{\alpha}} = -M^{\alpha} \left(\frac{\partial f^{\alpha}\left(\boldsymbol{u}, \phi_{\mathrm{c}}^{\alpha}, \nabla\phi_{\mathrm{c}}^{\alpha}\right)}{\partial\phi_{\mathrm{c}}^{\alpha}} - \mathrm{div}\left(\frac{\partial f^{\alpha}\left(\boldsymbol{u}, \phi_{\mathrm{c}}^{\alpha}, \nabla\phi_{\mathrm{c}}^{\alpha}\right)}{\partial\nabla\phi_{\mathrm{c}}^{\alpha}} \right) \right), \tag{25}$$

with a mobility $M^{\alpha} \geq 0$ is postulated. These evolution equations are defined on the subdomains Ω^{α}, whereas on the boundary $\partial\Omega^{\alpha}$ a homogeneous Neumann boundary condition with $\nabla\phi_{\mathrm{c}}^{\alpha} \cdot \boldsymbol{n} = 0$ applies. In contrast, the boundary $\mathcal{G}^{\alpha}$, resulting from the smooth transition of $\mathcal{G}$ (cf. Fig. 3), has to be treated separately. Neither a classical Neumann nor a Dirichlet boundary condition is a reasonable choice. A Neumann boundary condition would enforce a certain flux across the boundary. For example, a zero flux would result in a crack propagation direction perpendicular to the boundary. A Dirichlet boundary condition, on the other hand, would constrain the order parameter $\phi_{\mathrm{c}}^{\alpha}$ and thus the crack propagation. More complex boundary conditions, such as absorbing boundary conditions, or Robin type boundary conditions, could constitute more physical boundary conditions. Since these are neither widely used nor trivial to implement, an alternative approach is proposed: The evolution equation is extended to the whole domain Ω, but the elastic driving force is restricted to Ω^{α}, and considered to vanish anywhere else. This results in a continuous calculation of the crack order parameters, not restricted to the inner boundary, each with similar terms, as in the homogeneous model, but with phase-specific quantities. Outside the subdomain Ω^{α}, the phasefield is continued in the sense of the exponential profile (9), reproducing the correct sharp interface energy in a diffuse context. The coupling of these different equations takes place solely through the interpolation of the strain energy density. In addition, an irreversibility condition for each evolution equation is used: As in Section 2.1, each crack order parameter is kept damaged by means of the additional constraint $\phi_{\mathrm{c}}^{\alpha} = 1$, if $\phi_{\mathrm{c}}^{\alpha} \geq 0.99$.

2.4. Comparison

Classic homogeneous model. Section 2.1 introduced a crack propagation model based on established models from the literature. Many extensions and modifications to such a model can be found in the literature, which can improve the model for many applications [39,41,51]. Nevertheless, such extensions are avoided intentionally, reducing

Table 1
Comparison of the terms in the balance of linear momentum and the evolution equation of the SCOP and MCOP model. $\Delta\cdot$ denotes the Laplacian operator.

SCOP :	$\operatorname{div}\left(h(\phi_c)\sum_\alpha^N \phi^\alpha \boldsymbol{\sigma}^\alpha\right) = \mathbf{0}, \quad \dot{\phi}_c \frac{1}{M} = \sum_\alpha^N \phi^\alpha G_c^\alpha \left(\Delta\phi_c - \frac{1}{\epsilon_c^2}\phi_c\right) - \frac{1}{\epsilon_c}\frac{\partial h(\phi_c)}{\partial \phi_c}\sum_\alpha^N \phi^\alpha f_{el}^\alpha$
MCOP :	$\operatorname{div}\left(\sum_\alpha^N h(\phi_c^\alpha)\phi^\alpha \boldsymbol{\sigma}^\alpha\right) = \mathbf{0}, \quad \dot{\phi}_c^\alpha \frac{1}{M^\alpha} = G_c^\alpha \left(\Delta\phi_c^\alpha - \frac{1}{\epsilon_c^2}\phi_c^\alpha\right) - \frac{1}{\epsilon_c}\frac{\partial h(\phi_c^\alpha)}{\partial \phi_c^\alpha} f_{el}^\alpha, \quad \forall \alpha = 1, \dots, N$

the complexity, as the model is used as the basis for the introduced heterogeneous SCOP and MCOP models. In the scope of this work, no implementation of the classical model is conducted. While the limitations of the classical model are acknowledged, many of the established modifications might also be applied to the novel MCOP model, while retaining the advantages of this approach. Nevertheless, the classical model could be extended to heterogeneous systems, e.g. based on element-wise constant material properties in the context of the FEM. On the other hand, the SCOP model with the limit of a sharp interface would yield the same results.

Single-crack order parameter (SCOP) models. The SCOP model, introduced in Section 2.2, is similar to models from the literature [13,38,39]. However, there are some differences:

- Schneider et al. [13] introduced the order parameters ϕ^α and the crack order parameter ϕ_c in the same tuple $\boldsymbol{\phi}$. Therefore, ϕ_c also contributes to the summation condition (11). This results in a model where the phases show transitions to a common crack phase. In addition, the interpolation function $h(\phi_c)$ must then normalize with respect to $\sum_\alpha^N \phi^\alpha$, while the crack energy is also considered in the evaluation equation of the phases, and vice versa.
- Prajapati et al. [38] and Späth et al. [39] used a similar approach as Schneider et al. [13], but the crack evolution equation is assumed to be independent of the order parameters ϕ^α, and is solely used to determine effective material properties.
- In this work, the order parameters ϕ^α and the crack order parameter ϕ_c are introduced separately, and the damage of all phases is represented by ϕ_c, but without any phase transitions from these to the crack phase. This results in a model similar to Prajapati et al. [38] or Späth et al. [39], but without requiring a normalization of the interpolation function.
- Due to the similarities to established models, the SCOP model is used as a reference model in the following 2D examples.

SCOP vs MCOP model. Both models introduce a tuple of order parameters for the parametrization of the domain, thereby accounting for the heterogeneity of the body. The differences between both models are summarized in the following.

- *SCOP model:* Only a single crack order parameter is considered. Thus, all regions are equally damaged. Both, the balance of linear momentum as well as the evolution equation of the crack order parameter are obtained by minimization of the functional $\mathcal{F}$ with respect to the total domain Ω.
- *MCOP model:* A tuple of crack order parameters is introduced. Thus, the damage of a region is described by its own order parameter, which allows a more advanced degradation of the strain energy. Moreover, functionals $\mathcal{F}^\alpha$ are introduced on subdomains Ω^α. As for the SCOP model, the balance of linear momentum is obtained by the minimization of the total functional with respect to the total domain. However, the evolution equations of the crack order parameter are obtained by the minimization of the functionals $\mathcal{F}^\alpha$ with respect to the domain Ω^α of the corresponding crack order parameter. Each evolution equation also recovers the classic model, while maintaining a constant crack surface energy and many of the advantages of this model.

Furthermore, the differences in the evolution equations and linear momentum balances are summarized in Table 1.

3. Numerical treatment

Influence of the crack length parameter ϵ_c. Regarding phase-field crack models for simulations, it has been repeatedly shown that the length parameter used to determining the width of the diffuse transition between damaged material points and undamaged material points has an effect on the simulation results, see [19,20,39], for example. This is especially true when considering crack initiation processes, for which often ϵ_c is treated as material property, cf., e.g. Tanné et al. [65]. Recently, Kumar et al. [66] discussed crack nucleation in the context of phase-field modeling and promoted an alternative approach for nucleation treatment. If initial cracks exist and the transition width is compatible with the discretization grid and the domain size, the influence of ϵ_c is not significant [65,67–69]. This difficulty was extensively studied in [70], and it was concluded that the length parameter should be considered as a material property that depends on the tensile strength of a material. Tanné et al. [65] derived a possible solution for the correct determination of the length parameter. However, if the length parameter is considered as a material property, especially on small length scales, this often leads to difficulties, as the compatibility between the length parameter, the discretization grid, and the domain size is no longer guaranteed. To eliminate this sensitivity, Wu et al. [71] introduced an approach for brittle materials. Since the presented model is a completely new interpretation of the regularized crack problem, the approach by Wu et al.'s is not considered, to reduce complexity. For a clear presentation of the new model, the disadvantages and the problem of the dependence of the simulation results on the length parameter are acknowledged but not taken into account. However, improving of the model towards parameter insensitivity is nevertheless straight forward with the approach published in Wu et al. [71].

Algorithm 1: Staggered scheme for SCOP

```
initialize φ_c
initialize boundary condition
t ← t_0
while t < t_end do
    loop
        solve lin. momentum balance          // cf. Table 1
        solve evolution eq. for φ_c          // cf. Table 1
        φ_c ← φ_c + Δt φ̇_c
        adapt mesh
        static ← |φ̇_c|_∞ < ε_φc
        if static then
            t ← t + Δt
            increment boundary condition
            break
        end
    end
end
```

Algorithm 2: Staggered scheme for MCOP

```
initialize φ_c   ∀α = 1, ..., N
initialize boundary condition
t ← t_0
while t < t_end do
    loop
        solve lin. momentum balance          // cf. Table 1
        for α = 1 to N do
            solve evolution eq. for φ_c^α    // cf. Table 1
            φ_c^α ← φ_c^α + Δt φ̇_c^α
        end
        adapt mesh
        static ← max_{α=1,...,N} |φ̇_c^α|_∞ < ε_φc
        if static then
            t ← t + Δt
            increment boundary condition
            break
        end
    end
end
```

Numerical discretization. The proposed models result in a system of partial differential equations, consisting of the balance of linear momentum and multiple evolution equations for the crack order parameters. In this work the staggered approach of Miehe et al. [20] is used, which is based on a operator split. Each partial differential equation is solved by assuming the other fields constant. Together with a time stepping scheme

$$\phi_c^{n+1} = \phi_c^n + \Delta t \dot{\phi}_c, \qquad \phi_c^{\alpha,n+1} = \phi_c^{\alpha,n} + \Delta t \dot{\phi}_c^{\alpha}, \tag{26}$$

and a time step Δt, this results in linear partial differential equations. The index n denotes the order parameters for an old time step, while $n+1$ denotes the order parameter for a new time step.

In order to ensure a quasi-static crack propagation, the steady state conditions

$$\left|\dot{\phi}_c\right|_\infty < \epsilon_{\phi_c}, \qquad \left|\dot{\phi}_c^{\alpha}\right|_\infty < \epsilon_{\phi_c} \tag{27}$$

are introduced, with the infinity norm $|\cdot|_\infty$ and a tolerance parameter $\epsilon_{\phi_c} = 10^{-4}$. After solving the individual equations in each iteration, the condition is evaluated. Only if the condition is fulfilled, the system will progress

further in time. As a consequence there is an inner iteration loop, which solves each equation subsequently, until a steady state is reached, and an outer loop, which can be associated with a physical time and a time-dependent load, using boundary conditions. The procedure corresponding to this approach is illustrated as pseudocode in algorithm 1 for the SCOP model and compared to the MCOP model (algorithm 2). The mobilities M and M^α also reduce to numerical parameters and will not influence the results within a certain reasonable numerical range. In addition, an exemplary study of the evolution of these staggered systems and their iterations is conducted in Appendix A. In order to solve the partial differential equations, a FEM approach, based on the C++ finite element library *deal.II* [72], is used. In this work, first-order Lagrange finite elements and a second-order Gauss–Legendre quadrature rule for numerical integration are used. The evolution equations are solved using an implicit time stepping procedure (cf. Eq. (26)), except for the elastic driving force term, which is considered explicitly in time. Adaptive mesh refinement (AMR) is used to reduce the computational effort. Especially for the setup chosen in Section 4.2, big domains are required which are computationally unfeasible on a uniform mesh. In this work a basic AMR strategy is used, and the reader is referred to, for example, Heister et al. [54] for a more state-of-the-art AMR approach. The strategy of our current approach uses different criteria for refinement or coarsening for the evolution equation and the equilibrium of the linear momentum. Based on the gradient of the order parameter or strain energy density and the extent of the elements, discrete changes are calculated for each element. If certain values are exceeded or undershot, the element is refined, or coarsened, respectively. In addition, this procedure is explicitly evaluated in time. Despite limitations of the strategy acknowledged, it enables the computation of bigger domains. Combined with a very conservative refinement controlled by the values for refinement and coarsening, and frequent execution, the strategy has proven its robustness. However, this has the disadvantage of low computational optimization compared to more advanced approaches such as those of Heister et al. [54]. Nevertheless, it provides huge improvements over a uniform mesh.

Residual stiffness. For a FEM approach, an interpolation function $h(\phi_\mathrm{s})$, which will be zero for a fully broken state, will result in a singular stiffness and an ill-posed problem. This can be avoided by replacing the degradation function by

$$\tilde{h}(\phi_\mathrm{c}) = \begin{cases} h(\phi_\mathrm{c}) & 1-\phi_\mathrm{c} > \phi_\mathrm{s}^\mathrm{th}, \\ h\left(\phi_\mathrm{c}^\mathrm{th}\right) & \text{else}, \end{cases} \tag{28}$$

with a threshold value $\phi_\mathrm{s}^\mathrm{th} = 10^{-4}$. This function will preserve a certain value and even ensures a residual stiffness even for completely damaged regions.

4. Results

Effective crack order parameters. In order to be able to compare the results of the SCOP and MCOP model, additional effective order parameters are introduced. An order parameter ϕ^α can be decomposed into an effectively damaged part $\tilde{\phi}_\mathrm{c}^\alpha$ and an effectively undamaged part $\tilde{\phi}_\mathrm{s}^\alpha$:

$$\phi^\alpha = \tilde{\phi}_\mathrm{c}^\alpha + \tilde{\phi}_\mathrm{s}^\alpha. \tag{29}$$

Each of these parts is defined using the individual crack order parameters of the MCOP model

$$\tilde{\phi}_\mathrm{c}^\alpha = \phi^\alpha \phi_\mathrm{c}^\alpha, \qquad \tilde{\phi}_\mathrm{s}^\alpha = \phi^\alpha \left(1-\phi_\mathrm{c}^\alpha\right). \tag{30}$$

Also a totally effective crack order parameter is formulated:

$$\tilde{\phi}_\mathrm{c} = \sum_{\alpha=1}^{N} \tilde{\phi}_\mathrm{c}^\alpha. \tag{31}$$

Note that these effective quantities describe the damaged and the undamaged fraction with respect to $\sum_\alpha^N \phi^\alpha = 1$, which is in contrast to ϕ_c^α, which only describes the ratio of damage with respect to ϕ^α.

4.1. Steady-state profiles in 1D

To illustrate the difficulties of the heterogeneous SCOP model, steady-state profiles are examined for different model parameters and compared to the analytical solution. For the sake of simplicity, the system is assumed as

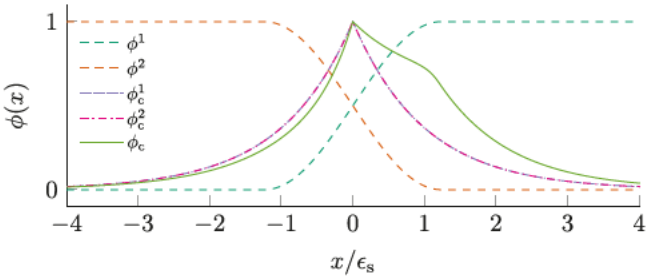

Fig. 4. Steady state profiles for a diffuse interface at $x = 0$, with $G_c^2/G_c^1 = 100$ and $\epsilon_c = \epsilon_s$.

binary and one-dimensional, while no mechanical loads are considered. Instead, a completely damaged point, in the middle of the domain, is placed and imposed via the boundary condition $\phi_c = 1$ or $\phi_c^\alpha = 1$, respectively. In addition, an interface with different critical energy release rates for both materials is also placed in the middle of the domain. In Fig. 4, exemplary steady-state profiles ϕ_c, for the SCOP model, and ϕ_c^α, for the MCOP model, are shown along with the imposed interface. Note that a high contrast of the crack surface energies $G_c^2/G_c^1 = 100$ and the same length parameters $\epsilon_c = \epsilon_s$ are chosen. This results in a highly distorted profile for the SCOP model, compared to the analytical profile, due to the additional spatial gradient in $\sum_\alpha^N \phi^\alpha G_c^\alpha$. In contrast, the evolution equations of the MCOP model are independent, as the coupling is modeled purely by the degradation of the strain energy density, which is not present here. Together with the constant G_c^α, this will avoid any distortions, and the analytical profile is reproduced.

The distorted profiles result in different energy densities and do not yield the analytically desired crack surface energy $G_c^* = 1/2\left(G_c^1 + G_c^2\right)$ when integrated over the domain. For the investigation of these deviations in the total energy, the error estimator deviation

$$e_{G_c} = \left| \frac{\mathcal{F} - G_c^*}{G_c^*} \right| \tag{32}$$

is introduced. For varying ratios of the critical energy release rates and interface widths, the deviations are displayed in Fig. 5(a). Due to the higher spatial gradient in the critical energy release rate, an increasing deviation for a higher contrast G_c^2/G_c^1, can be observed. For $\epsilon_s \gg \epsilon_c$, the change of the critical energy release rate is distributed over a larger physical width, leading to lower spatial gradients and lower deviations. If the case $\epsilon_s \ll \epsilon_c$ is considered, the spatial gradient increases, but its influence is limited to only a part of the crack interface, resulting in a relatively low deviation for the total energy of the system. From a numerical point of view, $\epsilon_s \approx \epsilon_c$ it is desired to reduce the effort of resolving both interfaces. In this case, however the deviation is rather high. The deviations shown here do not exceed $\approx 7.8\%$, which seems tolerable. Nevertheless, the maximum local deviation of the energy density can be defined by

$$e_f = \left. \frac{|f - f^*|}{f} \right|_{x=x_{\max}}, \tag{33}$$

with the analytical energy density f^*, defined by the analytical profile, and is evaluated at $x_{\max}$, for which the absolute difference of the density is highest. For the various parameters, this local deviation is shown in Fig. 5(b), which also shows an increasing deviation with higher G_c^2/G_c^1. With increasing ϵ_s/ϵ_c, the spatial gradient in $\sum_\alpha^N \phi^\alpha G_c^\alpha$ becomes more local, which also increase the deviations. For the MCOP model, the error quantities e_{G_c} and e_f will vanish, as the profiles are identical to the analytical ones and will reproduce the correct crack surface energy G_c^*.

Although a high contrast in the surface energies only produces moderate deviations in the total energy, the local deviations of the energy density are an order of magnitude higher. So far, no crack propagation behavior has been considered. However, it is expected that the inability of the SCOP model to reproduce the energy density and total crack surface energy will also influence the evolution of the crack, which will be investigated in the subsequent sections.

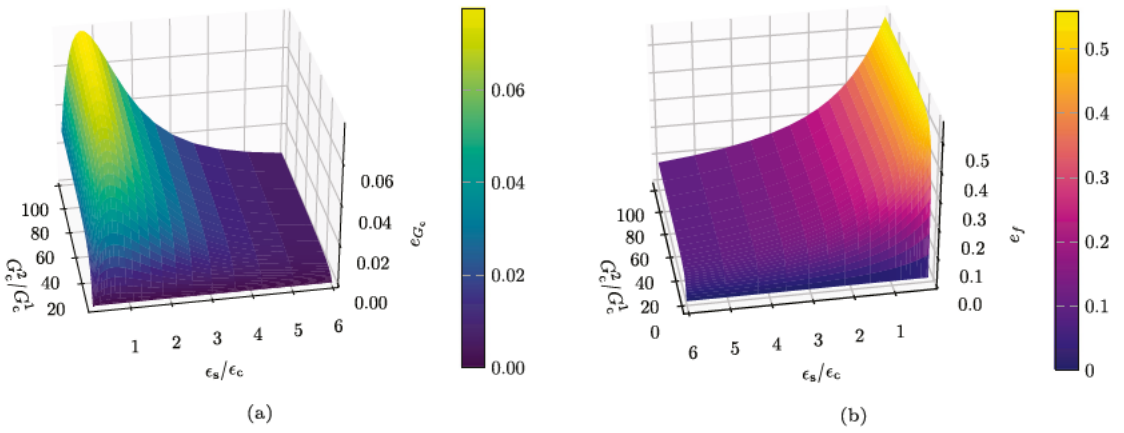

Fig. 5. (a) Error of the total crack energies e_{G_c}. (b) Maximum of the local error of the energy density e_f (b) and a diffuse interface with varying model parameters.

4.2. Sloped binary interface

This section follows the investigations by Henry [46]. Along with a binary interface, an initial crack is placed in a two-dimensional rectangular domain, with an angle θ between them, cf. Fig. 6. Note that the real size of the domain is large, compared to the interface widths, to avoid any influence from the boundaries.

In order to reduce complexity and avoid any influence of the chosen homogenization scheme, the elastic material behavior of both regions is assumed to be equal and isotropic with $\lambda^1 = \lambda^2$, $\mu^1 = \mu^2$. In his work, Henry imposed displacement boundary conditions, but in order to use the LEFM theory in the present work, stress boundary conditions are employed to apply an initial mode I crack opening. For a straight crack the stress intensity factor results from

$$K_\mathrm{I} = A\sigma\sqrt{a}, \tag{34}$$

with the generally unknown prefactor A, the crack length a, and the stress σ, far away from the crack, which hence is associated with the stress vector $\bar{t}$ of the boundary condition, cf. Fig. 6. If the stress is increased monotonously, this results in crack propagation above a critical stress, followed by an unstable crack growth. To be able to investigate the behavior of the crack propagation models, a quasi static crack growth with $K_\mathrm{I} = K_\mathrm{Ic}$ is desirable for a constant critical value K_Ic. To obtain such a stable crack growth, the applied stress will be increased after each time step. If the crack propagates, measured by an enlargement of the domain, $\phi_\mathrm{c} = 1$ holds, the stress at the boundaries is reduced below an estimated new critical value, which is based on the crack growth Δa. Furthermore, the stress increment for each time step is also reduced. This approach aims to achieve linear crack growth over time and avoid unstable crack growth.

Artificial interface. Firstly, the interface between the region is considered as artificial. Hence, the crack resistance is assumed to be equal, $G_\mathrm{c}^1 = G_\mathrm{c}^2$, resulting along with the same stiffness to the same material. The ratio of the interface width parameter of the solid and the crack is $\epsilon_\mathrm{c}/l_\mathrm{s} = 2/5$, and for the interface angle $\theta = 50°$ is chosen. The results after simulating a mode I crack propagation of such a system are shown in Fig. 7: It could be observed that the initial crack propagated straight through the domain, despite the presence of the interface. For the MCOP model, contour lines of the effective parts $\tilde{\phi}_\mathrm{c}^1$ and $\tilde{\phi}_\mathrm{c}^2$ are displayed, additionally. In the solid interface, the crack is transferred from one region to another, continuing the total effective crack, consisting of the sum of $\tilde{\phi}_\mathrm{c}^\alpha$. The resulting effective crack $\tilde{\phi}_\mathrm{c}$ of the MCOP model is comparable to ϕ_c of the SCOP model. In Fig. 8a, the temporal evolution of the crack length a, normalized by the initial crack length a_0, is plotted against the normalized simulation time. Here, both models also show the same effective behavior, and the transfer of the crack propagation, from one crack order parameter ϕ_c^α to the other, can be observed. The evolution of the applied stress σ, normalized by the critical stress to propagate the initial crack σ_0, is displayed in Fig. 8b. Because of the way the boundary condition

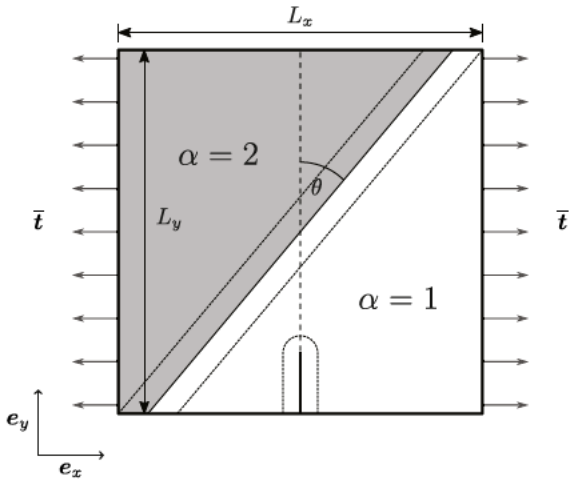

Fig. 6. Exemplary structure of an inclined interface, with an angle θ between the binary interface and the initial crack. A time-dependent stress is applied on the left and right boundary.

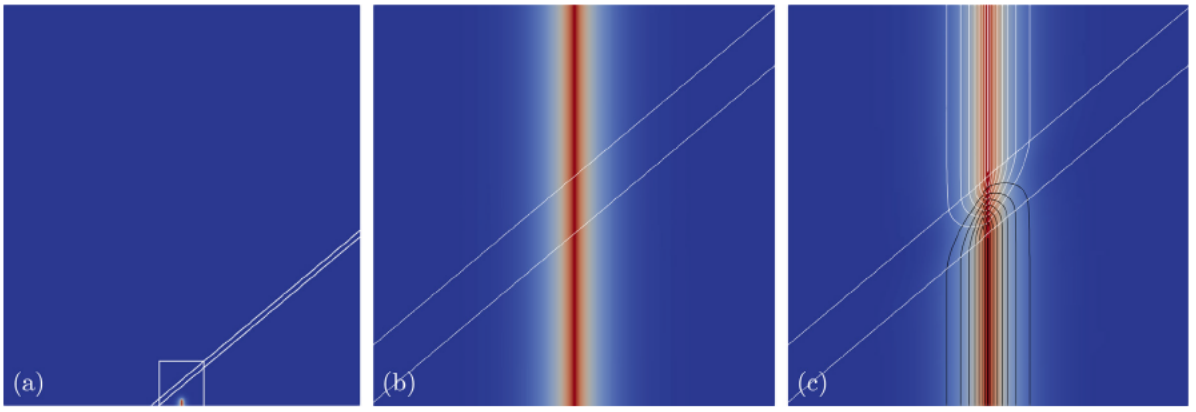

Fig. 7. Simulation domain with an initial crack and a marked and enlarged artificial interface region (a). The crack order parameter ϕ_c for the SCOP model (b) and $\bar{\phi}_c$ for the MCOP model (c), with contour lines for $\bar{\phi}_c^1$ and $\bar{\phi}_c^2$. In addition, the solid boundaries of the interface are shown.

is applied, it should be noted that only the time step is shown, in which the crack grows, while the other steps are omitted. The models show similar profiles and coincide with the expected profile from LEFM, cf. Eq. (34). Regardless of the use of multiple crack order parameters, the novel MCOP model is able to reproduce the crack path and kinetics of the SCOP model. Furthermore, the presented approach ensures quasi-static crack growth and produces an almost linear crack growth over time, as well as the desired relation between applied stress and crack length.

Infinitely tough region. The other limiting case of crack propagation with a binary interface is an infinitely tough interface, which can be obtained when $G_c^2 = \infty$, which ensures that the upper region cannot be damaged at all and enforces the crack to grow along the interface. For both regions, the same stiffness parameters are used, while the boundary condition is applied as before.

In Fig. 9, the crack path for both heterogeneous models and $\theta = 50°$ are shown, considering both a sharp solid interface (a–c) and a diffuse solid interface (d–f). The marked cross section is also drawn in Fig. 10 along with the solid interface. The SCOP model shows a non-physical behavior in some aspects:

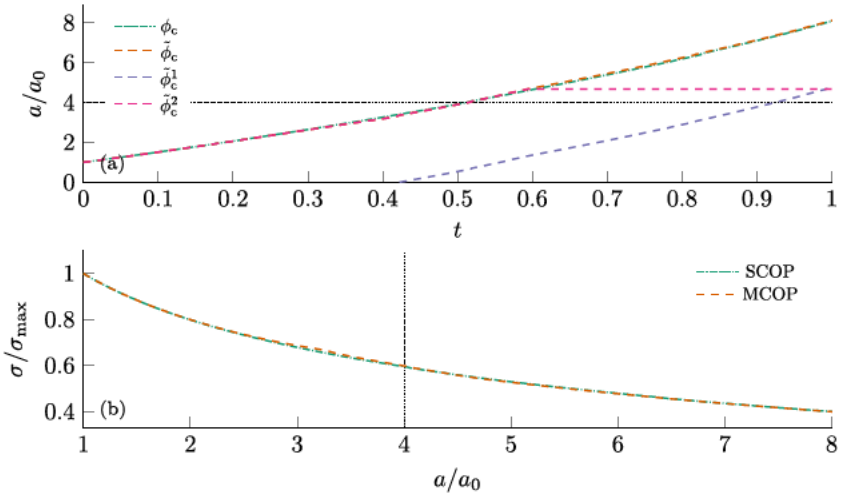

Fig. 8. Normalized temporal evolution of the crack length (a), and the stress at the boundary, applied against the crack length (b), for the SCOP and MCOP model with $\theta = 50°$.

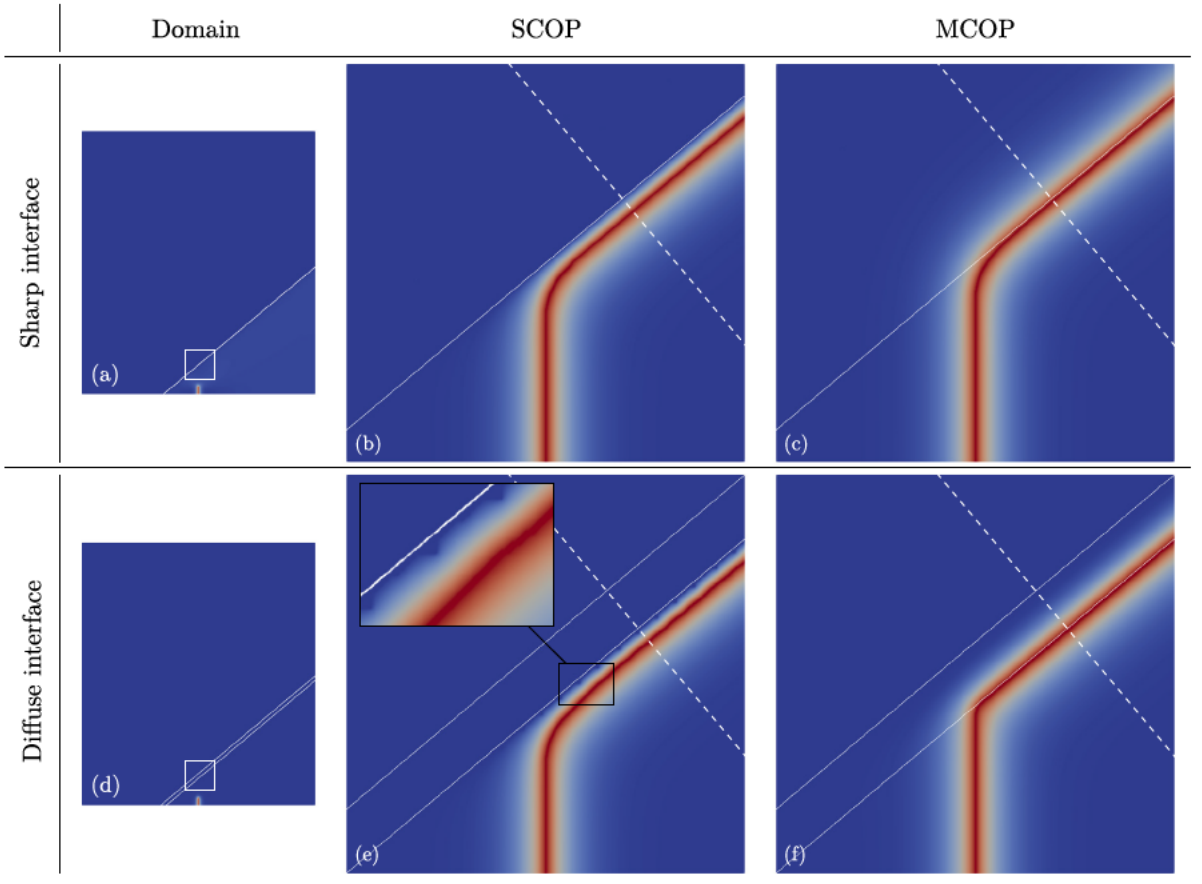

Fig. 9. Crack propagation along the sloped interface, for sharp and diffuse interfaces: Simulation domain with an initial crack and a marked and enlarged interface region (a,d). The crack order parameter ϕ_c for the SCOP model (b,e) and $\tilde{\phi}_c$ for the MCOP model (c, f), after the crack propagated along the infinitely tough interface. In addition, the solid boundaries of the interface and the cross-section of Fig. 10 are shown.

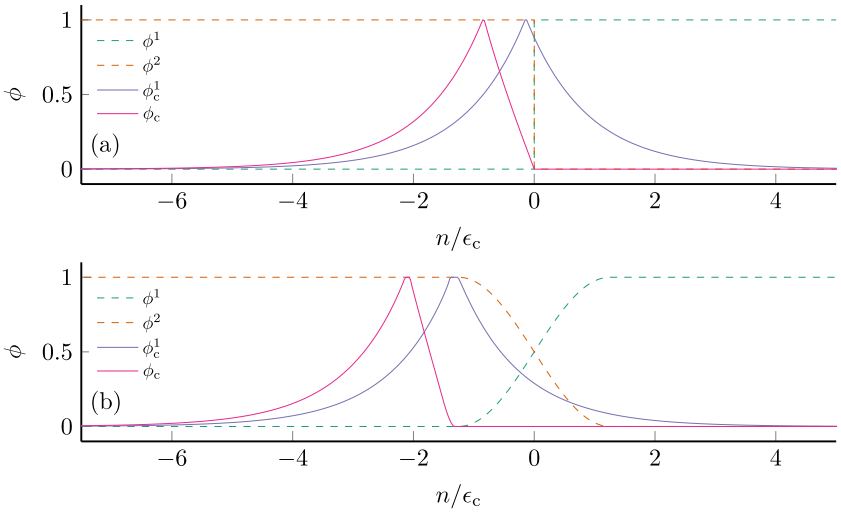

Fig. 10. Cross-section with the underlying solid interface, along the binary interface of the SCOP and MCOP model, shown in Fig. 9, for a sharp (a) and diffuse interface (b).

- Due to the interpolation of the individual critical energy release rates G_c^α and the infinitely tough upper region, no crack can occur there or in the interface region. This constrains the crack propagation in such a way that the crack is deflected before it reaches the solid interface.
- This interpolation also causes problems as to how the crack grows along the interface. Because the order parameter in the interface must be zero, this leads to a certain distance of the crack from the interface.
- For the diffuse interface, the high gradients of ϕ_c towards the interface combined with the nonconforming mesh cause numerical issues, leading to numerical artifacts, as shown in the magnification of Fig. 9b. Regarding the sharp interface, which requires a conforming mesh, these artifacts are not present.

In contrast, the MCOP model exhibits fewer of these difficulties: For the diffuse interface, the crack grows straight up to the interface, where it performs distinct deflection. The deflection is less pronounced for the sharp interface due to the loss of the driving force immediately beyond the interface. However, for both the diffuse and sharp interfaces, the crack continues directly at the edge of the interface, and the crack exhibits the desired analytical profile of the diffuse interface, as illustrated in Fig. 10.

For a quantitative comparison of the models, the approach of Henry [46] and the analytical analysis of Amestoy and Leblond [4] are used and briefly introduced, in the following. The stress intensity factors for the crack modes I and II of the straight crack, i.e., before the deflection of the crack at the interface, result from

$$K_\mathrm{I} = A\sigma_0\sqrt{a}, \qquad K_\mathrm{II} = 0. \tag{35}$$

In contrast, the stress intensity factors can be described by

$$\hat{K}_\mathrm{I} = f(\theta)K_{\mathrm{I}0}, \qquad \hat{K}_\mathrm{II} = g(\theta)K_{\mathrm{I}0}, \tag{36}$$

directly after the kink of the crack path, where $f(\theta)$ and $g(\theta)$ are given by Amestoy and Leblond [4]. $K_{\mathrm{I}0}$ is the stress intensity factor right before the kink of the mode I crack. The energy release rates after the kink $\hat{G}$ result from

$$\hat{G} = \frac{\hat{K}_\mathrm{I}^2 + \hat{K}_\mathrm{II}^2}{E'}, \tag{37}$$

while the ratio of $\hat{G}$ and the energy release rates before the kink G_0 can be expressed using the analytical solution

$$\frac{\hat{G}}{G_0} = f(\theta)^2 + g(\theta)^2, \tag{38}$$

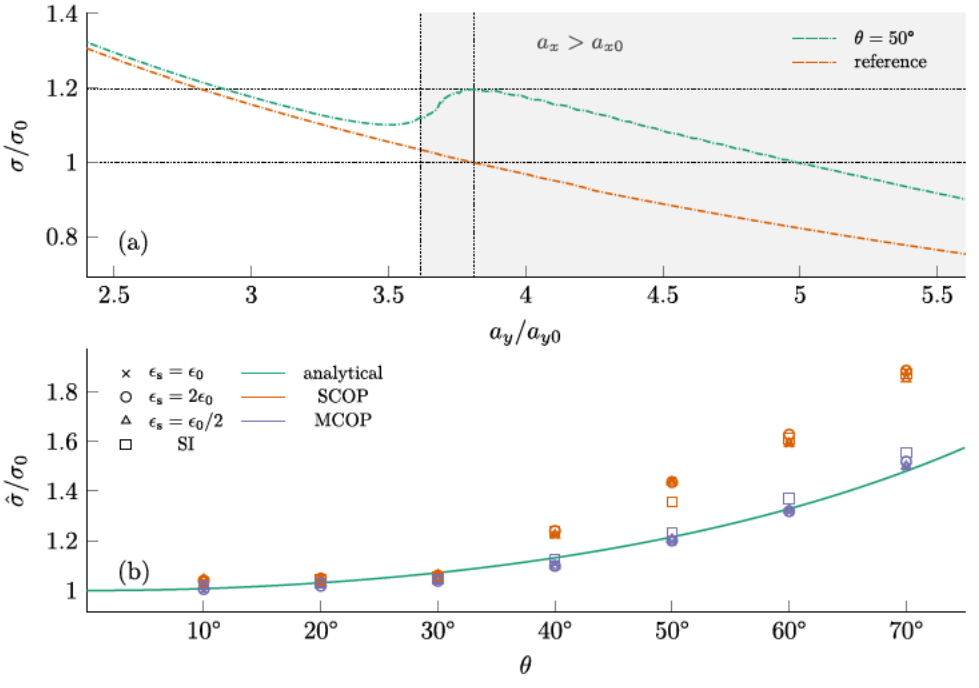

Fig. 11. Exemplary visualization of the evaluation of the crack propagation (a) and comparison with an analytical solution for the SCOP and MCOP model (b), for a crack propagating along an infinitely tough interface, with a different angle θ. Various solid length parameters ϵ_s as well as a sharp interface (SI) are examined.

with $E' = E/(1-\nu^2)$. With Eq. (35), this ratio can also be given by

$$\frac{\hat{G}}{G_0} = \left(\frac{\hat{\sigma}}{\sigma_0}\right)^2, \tag{39}$$

using the applied stress at the interface after the kink $\hat{\sigma}$, and a reference stress σ_0, representing the stress of a straight crack with the same crack length in the y-direction. In Fig. 11a, an exemplary illustration of the evaluation procedure is given. When the crack hits the interface, the critical stress for propagation increases, which can be observed by a peak in the graph. By determining the maximum value of this peak for which $a_x > a_{x0}$ holds, and comparing it with the reference stress $\hat{\sigma}$ of a simulation without a solid interface but with the same crack length in the y-direction a_y, a comparison with the analytical solution is possible. In Fig. 11b, this procedure was conducted for both models, several angles, sharp and diffuse interfaces. For small angles, both approaches show a fairly good agreement with the analytical solution. For higher angles, however, the SCOP model strongly differs from the solution, while the MCOP model still agrees with the analytical solution from the LEFM. Note that a variation of the width of the solid interface was also conducted, where the sharp interface can be considered as a limiting case. Neither increasing nor decreasing of the interface width has any significant effect on the results. For a mesh convergence study of this setup the reader is referred to Appendix B.

In conclusion, regarding the SCOP model, neither the crack grows to the interface, nor the model is able to reproduce the stress increase at which crack propagation occurs along the inclined interface. In contrast, the MCOP model propagates to the interface, develops more significant deflection, and predicts the increase in stress according to theory. Regarding the comparison with sharp solid interfaces, no significant differences could be found. This limits the novel MCOP model not only to the application at diffuse interfaces, but also allows for the application to sharp interfaces. Concerning the diffuse boundary approach, both SCOP and MCOP avoid the need for conforming meshes. However, the MCOP model offers the possibility to extend the homogenization scheme, e.g., by considering jump conditions [13,73].

Table 2
Material properties (a) and interface width parameters (b) for simulating the fracture of FRP volume elements.

Material	Elasticity			Fracture
	E	ν	Reference	G_c
Thermoset	3.45 GPa	0.38	[74]	100.0 J m^{-2}
Glass fiber	73.0 GPa	0.22	[75]	200.0 J m^{-2}

(a)

Parameter	Value
l_s	1 µm
ϵ_c	1.25 µm

(b)

4.3. Application to FRPs

In the previous numerical studies, the same elastic material behavior has been assumed for both regions. But realistic systems with a high contrast in crack resistance will most likely also have a high contrast in their elastic parameters. In this section, a fiber-reinforced polymer (FRP) is chosen to schematically demonstrate the ability of the novel MCOP model to illustrate crack propagation behavior in the context of a material with heterogeneous elastic properties. A quantitative analysis of the results is omitted, as this would most likely require an extension of the model, e.g., a state-of-the-art tension–compression splitting, or accounting for interfacial crack propagation, which is beyond the scope of this work.

The matrix consists of a UPPH resin system [76], reinforced by glass fibers. The material parameters for both materials are given in Table 2a, while the interfacial widths used are shown in Table 2b. FRPs exhibit a complex fracture behavior: Either the matrix may fail, the fibers may break, or the material may fail due to the debonding of the interface. To investigate crack propagation in such a material, volume elements with a certain fiber volume content, orientation, and periodicity are considered. Boundary conditions, such as normal Neumann or Dirichlet types, do not account for the periodicity of the domain. Hence a periodic type is chosen: In addition to the periodic order parameters and displacement fields, a superimposed periodic displacement boundary condition [77] is applied in such a way that the macroscopic strain of the volume element follows by

$$\overline{\boldsymbol{\varepsilon}} = \varepsilon(t)\boldsymbol{e}_x \otimes \boldsymbol{e}_x, \tag{40}$$

where the normal strain in the x-direction, $\varepsilon(t)$, will be increased linearly with time, until the volume element exhibits a complete failure.

Unidirectional 2D volume elements. First, unidirectional fiber reinforced volume elements are be investigated. This makes it possible to reduce the system to a 2D system, so as to reduce the computational effort. The square volume elements with a side length of 100 µm contains fibers with a radius of 4 µm. For different fiber volume fractions v_f, various realizations will be considered in the following. In Fig. 12, the effective crack $\tilde{\phi}_c$ and the contour lines of the fibers are presented in a fully broken state. All realizations show an overall crack direction, perpendicular to the applied load. Thus, the desired and dominant crack opening mode I is reproduced, and the crack paths tend to become more complex, when using a higher fiber volume fraction, as the fibers become an obstacle for the crack, which results in an elongation and contortion of the crack path. This is primarily caused by the lower crack resistance of the matrix. Thus, the crack also often propagates through matrix-dominated regions, but also between fibers caused by stress concentration. Since the MCOP model does not account for the failure mechanism of interfacial debonding, this failure mechanism cannot be observed when the crack propagates in fiber dominated regions. Due to the periodic boundaries, the complete failure of the volume element forces the crack tips to merge. After the merge, partly 'dead ends' can thus be observed in some realizations presented in this work.

Isotropic 3D volume element. In the case of a 3D volume element, the fiber volume content $v_f = 25\%$ is chosen with an isotropic orientation distribution. The latter implies that there is no preferential direction in the fiber distribution. As before, the volume element has a side length of 100 µm, consisting of fibers with a radius of 4 µm and a length of 80 µm. The volume element was generated using the approach of Schneider et al. [78] and is shown in Fig. 13(a). As in the 2D case, a macroscopic strain is applied in one direction, in addition to the periodicity, and is increased linearly over time. The failed domain with the red crack surface is shown in Fig. 13(b). As for the 2D simulations the crack surface is mainly perpendicular to the load direction and occurs solely in the matrix, but still shows a quite complex crack path, due to the fiber distribution and the stress concentration that arise from it.

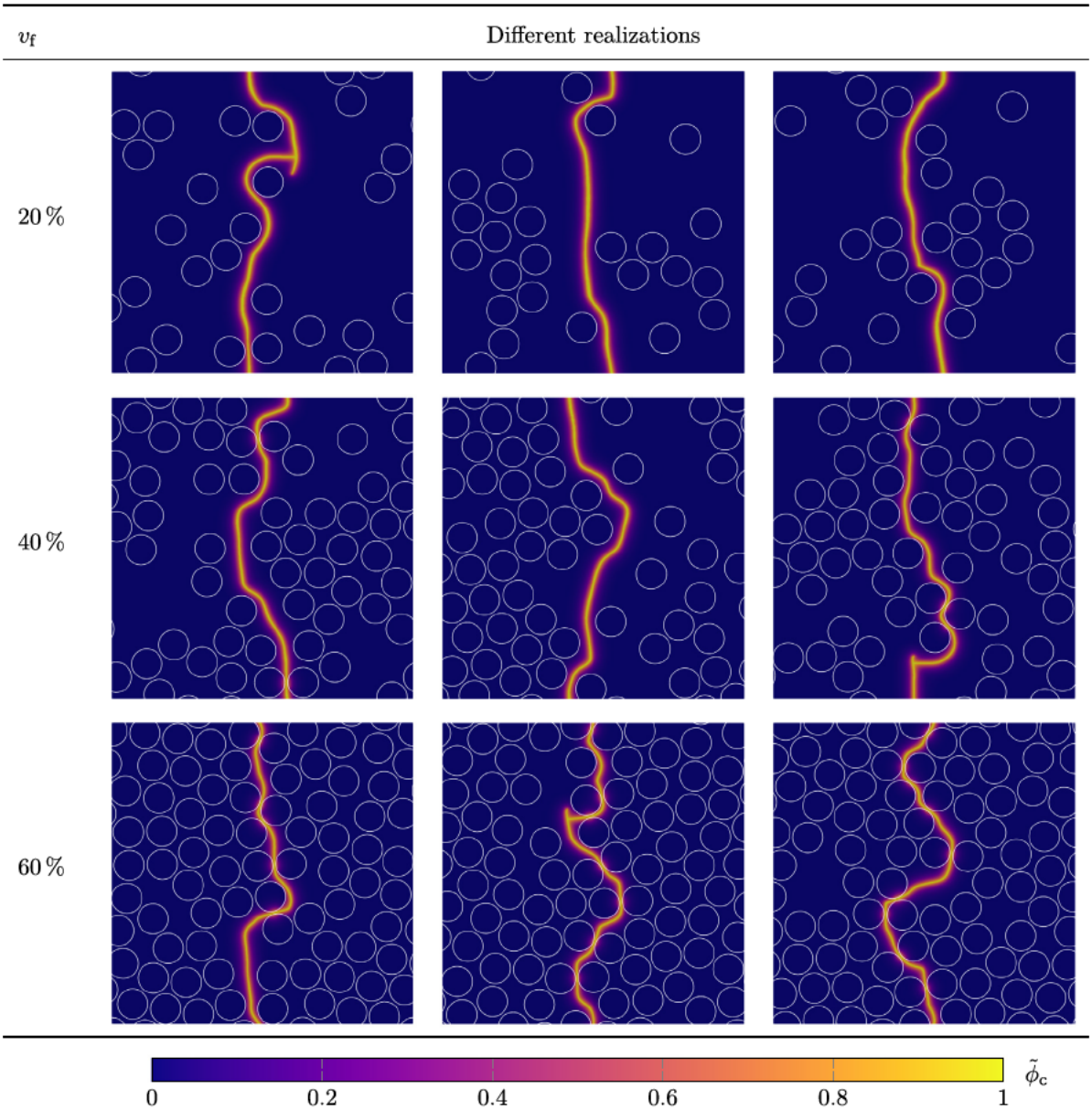

Fig. 12. Different realizations of randomly generated periodic 2D volume elements with unidirectional fibers for varying fiber volume fractions v_f. Additionally, the effective crack $\tilde{\phi}_c$, after uniaxial strain and failure is shown.

5. Conclusion

In this work, two different phase-field models for crack propagation in heterogeneous systems were introduced and compared:

- A SCOP model, based on established approaches, which uses a single crack order parameter to account for damage.

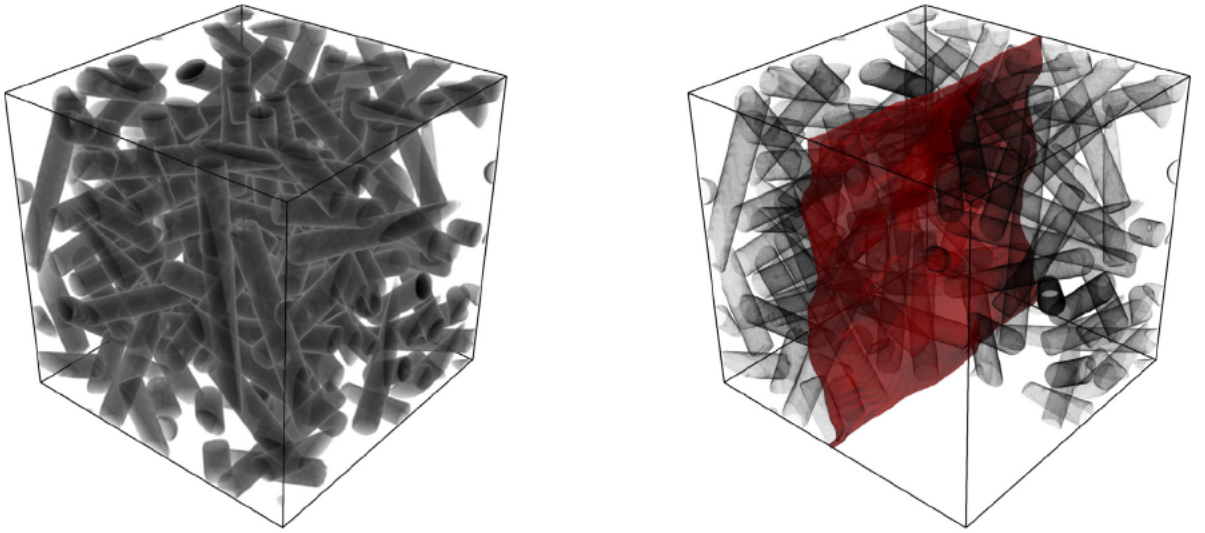

Fig. 13. A randomly generated periodic 3D volume element with isotropic fiber distribution (a) and the fractured volume element after applying a uniaxial strain, highlighted by a red crack surface (b).

- A novel MCOP model, that introduces multiple order parameters in order to distribute the effective damage to the individual regions, modeled by its own set of order parameters. This results in multiple evolution equations, each of which has a constant crack surface energy.

It was shown that the SCOP model is not able to reproduce the surface energy of the sharp interface for an interfacial crack, especially when the same length parameters are chosen for the solid and crack problem. In comparison, the novel MCOP formulation avoids any errors in that case. Furthermore, the model demonstrated the same kinetics and crack profiles during the propagation though an artificial interface, which confirms that multiple crack order parameters can generate a continuously effective crack.

An extension to an infinitely tough interface indicated further problems with the SCOP model, as the crack is deflected from the interface before it hits the interface itself, and maintains a certain distance from it. In contrast, the novel MCOP model demonstrates a more pronounced kink of the crack path at the interface and grows directly along the interface, for both sharp and diffuse interfaces. A quantitative comparison between the models for different angles of the interface and an analytical solution also showed a huge improvement in the modeling of crack propagation in heterogeneous materials: In particular, for high angles of the interface the SCOP model cannot replicate the analytical solution, where the MCOP model still shows very good agreement with it.

The application of the novel model to FRP for unidirectional fibers in 2D and the extension to a 3D domain with isotropic fiber orientation distribution shows that the ability is able to depict crack evolution in such a complex system, including crack nucleation and merging.

Notwithstanding the fact that the crack phase-field model avoids established extensions, such as a tension–compression splitting or the removal of the interface parameter dependence, the many remaining advantages of using multiple crack order parameters could be demonstrated. In future work, a tension–compression split, for example based on the work of Storm et al. [51], combined with a more advanced homogenization scheme based on the work of Schneider et al. [36], could further improve the model. In addition, a combination with a solid–solid phasefield transition model and plasticity could allow the study of other material systems, e.g., crack evolution during martensitic phase transformation [79]. The inclusion of an interfacial crack resistance could also allow for a more sophisticated simulation of FRP failure, by enabling realistic fiber debonding.

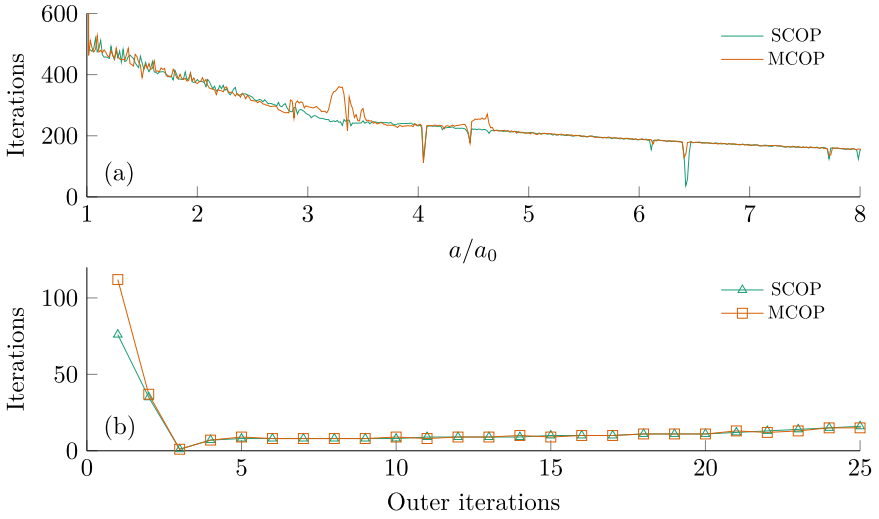

Fig. A.14. Behavior of the staggered scheme for the artificial sloped interface: (a) Cumulative iterations during the crack growth for the SCOP and MCOP models. (b) Amount of inner iterations for an exemplary discrete crack propagation step.

Declaration of competing interest

The authors declare that they have no known competing financial interests or personal relationships that could have appeared to influence the work reported in this paper.

Acknowledgments

We thank the German Research Foundation (DFG) for funding main parts of the model development within a partial project of the International Research Training Group IRTG 2078. Furthermore, contributions regarding the theoretical derivations have been provided through funding by the German Research Foundation (DFG) under Project ID 390874152 (POLiS Cluster of Excellence) and CELEST (Center for Electrochemical Energy Storage Ulm–Karlsruhe). Support of the Helmholtz program “Material Systems Engineering (MSE)”, topic 1 (43.31.01) and the KIT strategy of excellence, future fields project “KaDI4Mat” for data analysis, evaluation of results and integration in data workflows within the research data infrastructure Kadi4Mat is gratefully acknowledged.

Appendix A. Staggered iterations study

For a numerical investigation of the number of staggered iterations during a crack propagation simulation, the setup of an artificial sloped interface, cf. Section 4.2, is chosen. For this purpose, the number of iterations is depicted in Fig. A.14. The cumulative iterations over the crack growth are shown in Fig. A.14a. For this purpose, all inner staggered iterations are summed up until a discrete crack propagation occurs. Thereby, the SCOP and MCOP models show similar behavior. The number of iterations is approximately equal. Only near the solid interface the MCOP requires more iterations. This is most likely due to the implicit transition of the crack from one order parameter to the other. The overall trend towards fewer iterations, like the change in slope, is likely due to the way the stress boundary condition is imposed. In addition, Fig. A.14b plots the number of staggered iterations against temporal iterations for a discrete crack propagation step. Also here, SCOP and MCOP show the similar behavior: After a discrete crack propagation, the first iterations consist of an increased number of staggered iterations, while subsequently, the iterations are lower, but increase slightly again to the next discrete crack propagation.

Appendix B. Mesh convergence study

For an investigation of mesh convergence for the artificial sloped interface example (cf. Section 4.2), the SCOP model and the infinitely hard upper region are chosen. As in this case the highest gradients occur in the solution fields and can therefore be assumed to be the most challenging problem to discretize. Fig. B.15 shows the results

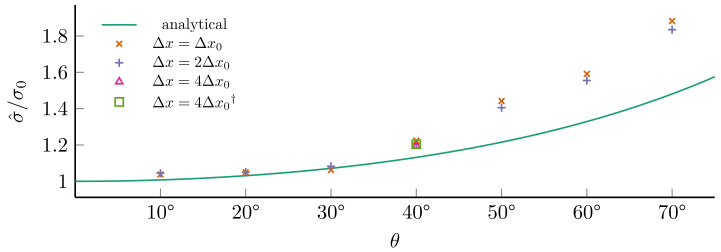

Fig. B.15. Mesh convergence study of the SCOP model for the artificial sloped interface: The mesh sizes at the crack tip Δx are varied. In addition, the background was also refined and the adaptive mesh refinement parameters were chosen more cautiously (†).

of the SCOP model of Section 4.2. In addition, the mesh size Δx at the crack tip is varied, where Δx_0 is the size in of the previous results. Furthermore, the underlying coarse mesh is significantly refined, and the adaptive mesh refinement parameters are changed to increase the area where Δx applies, denoted by † in Fig. B.15. Thereby, none of the results yields large variance, therefore the discretization chosen in this work can be assumed to be representative.

References

[1] L.B. Freund, Dynamic Fracture Mechanics, Cambridge University Press, 1990, http://dx.doi.org/10.1017/CBO9780511546761.
[2] B. Lawn, Fracture of Brittle Solids, Cambridge University Press, 1993, http://dx.doi.org/10.1017/cbo9780511623127.
[3] H. Ming-Yuan, J.W. Hutchinson, Crack deflection at an interface between dissimilar elastic materials, Int. J. Solids Struct. 25 (9) (1989) 1053–1067, http://dx.doi.org/10.1016/0020-7683(89)90021-8.
[4] M. Amestoy, J.B. Leblond, Crack paths in plane situations-II. Detailed form of the expansion of the stress intensity factors, Int. J. Solids Struct. 29 (4) (1992) 465–501, http://dx.doi.org/10.1016/0020-7683(92)90210-K.
[5] G.I. Barenblatt, The formation of equilibrium cracks during brittle fracture. General ideas and hypotheses. Axially-symmetric cracks, J. Appl. Math. Mech. 23 (3) (1959) 622–636, http://dx.doi.org/10.1016/0021-8928(59)90157-1.
[6] D.S. Dugdale, Yielding of steel sheets containing slits, J. Mech. Phys. Solids 8 (2) (1960) 100–104, http://dx.doi.org/10.1016/0022-5096(60)90013-2.
[7] M. Elices, G.V. Guinea, J. Gómez, J. Planas, The cohesive zone model: advantages, limitations and challenges, Eng. Fract. Mech. 69 (2) (2001) 137–163, http://dx.doi.org/10.1016/S0013-7944(01)00083-2.
[8] T.P. Fries, T. Belytschko, The extended/generalized finite element method: An overview of the method and its applications, Internat. J. Numer. Methods Engrg. 84 (3) (2010) 253–304, http://dx.doi.org/10.1002/nme.2914.
[9] A. Prahs, T. Böhlke, On interface conditions on a material singular surface, Contin. Mech. Thermodyn. 32 (5) (2020) 1417–1434, http://dx.doi.org/10.1007/S00161-019-00856-1.
[10] L.-Q. Chen, Phase-Field Models for Microstructure Evolution, Annu. Rev. Mater. Res. 32 (1) (2002) 113–140, http://dx.doi.org/10.1146/annurev.matsci.32.112001.132041.
[11] N. Moelans, B. Blanpain, P. Wollants, An introduction to phase-field modeling of microstructure evolution, Calphad: Comput. Coupling Phase Diagr. Thermochem. 32 (2) (2008) 268–294, http://dx.doi.org/10.1016/j.calphad.2007.11.003.
[12] B. Nestler, A. Choudhury, Phase-field modeling of multi-component systems, Curr. Opin. Solid State Mater. Sci. 15 (3) (2011) 93–105, http://dx.doi.org/10.1016/j.cossms.2011.01.003.
[13] D. Schneider, O. Tschukin, A. Choudhury, M. Selzer, T. Böhlke, B. Nestler, Phase-field elasticity model based on mechanical jump conditions, Comput. Mech. 55 (5) (2015) 887–901, http://dx.doi.org/10.1007/s00466-015-1141-6.
[14] C. Herrmann, E. Schoof, D. Schneider, F. Schwab, A. Reiter, M. Selzer, B. Nestler, Multiphase-field model of small strain elasto-plasticity according to the mechanical jump conditions, Comput. Mech. 62 (6) (2018) 1399–1412, http://dx.doi.org/10.1007/s00466-018-1570-0.
[15] A. Karma, D.A. Kessler, H. Levine, Phase-Field Model of Mode III Dynamic Fracture, Phys. Rev. Lett. 87 (4) (2001) 45501–1–45501–4, http://dx.doi.org/10.1103/PhysRevLett.87.045501.
[16] R. Spatschek, M. Hartmann, E. Brener, H. Müller-Krumbhaar, K. Kassner, Phase Field Modeling of Fast Crack Propagation, Phys. Rev. Lett. 96 (1) (2006) 015502, http://dx.doi.org/10.1103/PhysRevLett.96.015502.
[17] H. Henry, H. Levine, Dynamic Instabilities of Fracture under Biaxial Strain Using a Phase Field Model, Phys. Rev. Lett. 93 (10) (2004) 105504, http://dx.doi.org/10.1103/PhysRevLett.93.105504.
[18] B. Bourdin, G.A. Francfort, J.J. Marigo, Numerical experiments in revisited brittle fracture, J. Mech. Phys. Solids 48 (4) (2000) 797–826, http://dx.doi.org/10.1016/S0022-5096(99)00028-9.
[19] C. Kuhn, R. Müller, A continuum phase field model for fracture, Eng. Fract. Mech. 77 (18) (2010) 3625–3634, http://dx.doi.org/10.1016/j.engfracmech.2010.08.009.

[20] C. Miehe, M. Hofacker, F. Welschinger, A phase field model for rate-independent crack propagation: Robust algorithmic implementation based on operator splits, Comput. Methods Appl. Mech. Engrg. 199 (45–48) (2010) 2765–2778, http://dx.doi.org/10.1016/j.cma.2010.04.011.
[21] A.A. Griffith, VI. The phenomena of rupture and flow in solids, Philos. Trans. R. Soc. London Ser. A 221 (582–593) (1921) 163–198, http://dx.doi.org/10.1098/rsta.1921.0006.
[22] G.A. Francfort, J.J. Marigo, Revisiting brittle fracture as an energy minimization problem, J. Mech. Phys. Solids 46 (8) (1998) 1319–1342, http://dx.doi.org/10.1016/S0022-5096(98)00034-9.
[23] G.A. Francfort, B. Bourdin, J.J. Marigo, The Variational Approach to Fracture, J. Elasticity 91 (1–3) (2008) 5–148, http://dx.doi.org/10.1007/s10659-007-9107-3.
[24] C. Herrmann, D. Schneider, E. Schoof, F. Schwab, B. Nestler, Phase-Field Model for the Simulation of Brittle-Anisotropic and Ductile Crack Propagation in Composite Materials, Materials 14 (17) (2021) http://dx.doi.org/10.3390/ma14174956.
[25] M. Ambati, T. Gerasimov, L. De Lorenzis, Phase-field modeling of ductile fracture, Comput. Mech. 55 (5) (2015) 1017–1040, http://dx.doi.org/10.1007/s00466-015-1151-4.
[26] M. Ambati, L. De Lorenzis, Phase-field modeling of brittle and ductile fracture in shells with isogeometric NURBS-based solid-shell elements, Comput. Methods Appl. Mech. Engrg. 312 (2016) 351–373, http://dx.doi.org/10.1016/j.cma.2016.02.017.
[27] C. Kuhn, T. Noll, R. Müller, On phase field modeling of ductile fracture, GAMM-Mitt. 39 (1) (2016) 35–54, http://dx.doi.org/10.1002/gamm.201610003.
[28] D. Schneider, M. Selzer, J. Bette, I. Rementeria, A. Vondrous, M.J. Hoffmann, B. Nestler, Phase-Field Modeling of Diffusion Coupled Crack Propagation Processes, Adv. Energy Mater. 16 (2) (2014) 142–146, http://dx.doi.org/10.1002/adem.201300073.
[29] C. Miehe, L.M. Schänzel, H. Ulmer, Phase field modeling of fracture in multi-physics problems. Part I. Balance of crack surface and failure criteria for brittle crack propagation in thermo-elastic solids, Comput. Methods Appl. Mech. Engrg. 294 (2015) 449–485, http://dx.doi.org/10.1016/j.cma.2014.11.016.
[30] C. Miehe, M. Hofacker, L.M. Schänzel, F. Aldakheel, Phase field modeling of fracture in multi-physics problems. Part II. Coupled brittle-to-ductile failure criteria and crack propagation in thermo-elastic-plastic solids, Comput. Methods Appl. Mech. Engrg. 294 (2015) 486–522, http://dx.doi.org/10.1016/j.cma.2014.11.017.
[31] T. Wick, Multiphysics Phase-Field Fracture: Modeling, Adaptive Discretizations, and Solvers, De Gruyter, 2020, http://dx.doi.org/10.1515/9783110497397.
[32] B. Li, C. Peco, D. Millán, I. Arias, M. Arroyo, Phase-field modeling and simulation of fracture in brittle materials with strongly anisotropic surface energy, Internat. J. Numer. Methods Engrg. 102 (3–4) (2015) 711–727, http://dx.doi.org/10.1002/nme.4726.
[33] T.T. Nguyen, J. Réthoré, J. Yvonnet, M.C. Baietto, Multi-phase-field modeling of anisotropic crack propagation for polycrystalline materials, Comput. Mech. 60 (2) (2017) 289–314, http://dx.doi.org/10.1007/s00466-017-1409-0.
[34] C. Kuhn, R. Müller, A discussion of fracture mechanisms in heterogeneous materials by means of configurational forces in a phase field fracture model, Comput. Methods Appl. Mech. Engrg. 312 (2016) 95–116, http://dx.doi.org/10.1016/j.cma.2016.04.027.
[35] M.Z. Hossain, C.J. Hsueh, B. Bourdin, K. Bhattacharya, Effective toughness of heterogeneous media, J. Mech. Phys. Solids 71 (1) (2014) 15–32, http://dx.doi.org/10.1016/j.jmps.2014.06.002.
[36] D. Schneider, E. Schoof, Y. Huang, M. Selzer, B. Nestler, Phase-field modeling of crack propagation in multiphase systems, Comput. Methods Appl. Mech. Engrg. 312 (2016) 186–195, http://dx.doi.org/10.1016/j.cma.2016.04.009.
[37] B. Nestler, H. Garcke, B. Stinner, Multicomponent alloy solidification: Phase-field modeling and simulations, Phys. Rev. E 71 (4) (2005) 041609, http://dx.doi.org/10.1103/PhysRevE.71.041609.
[38] N. Prajapati, C. Herrmann, M. Späth, D. Schneider, M. Selzer, B. Nestler, Brittle anisotropic fracture propagation in quartz sandstone: insights from phase-field simulations, Comput. Geosci. 24 (3) (2020) 1361–1376, http://dx.doi.org/10.1007/s10596-020-09956-3.
[39] M. Späth, C. Herrmann, N. Prajapati, D. Schneider, F. Schwab, M. Selzer, B. Nestler, Multiphase-field modelling of crack propagation in geological materials and porous media with Drucker-Prager plasticity, Comput. Geosci. 25 (2020) 1–19, http://dx.doi.org/10.1007/s10596-020-10007-0.
[40] A.C. Hansen-Dörr, R. de Borst, P. Hennig, M. Kästner, Phase-field modelling of interface failure in brittle materials, Comput. Methods Appl. Mech. Engrg. 346 (2019) 25–42, http://dx.doi.org/10.1016/j.cma.2018.11.020.
[41] A.C. Hansen-Dörr, F. Dammaß, R. de Borst, M. Kästner, Phase-field modeling of crack branching and deflection in heterogeneous media, Eng. Fract. Mech. 232 (2020) 107004, http://dx.doi.org/10.1016/j.engfracmech.2020.107004.
[42] T.T. Nguyen, J. Yvonnet, Q.Z. Zhu, M. Bornert, C. Chateau, A phase-field method for computational modeling of interfacial damage interacting with crack propagation in realistic microstructures obtained by microtomography, Comput. Methods Appl. Mech. Engrg. 312 (2016) 567–595, http://dx.doi.org/10.1016/j.cma.2015.10.007.
[43] M. Paggi, J. Reinoso, Revisiting the problem of a crack impinging on an interface: A modeling framework for the interaction between the phase field approach for brittle fracture and the interface cohesive zone model, Comput. Methods Appl. Mech. Engrg. 321 (2017) 145–172, http://dx.doi.org/10.1016/j.cma.2017.04.004.
[44] R. Dimitri, P. Cornetti, V. Mantič, M. Trullo, L. De Lorenzis, Mode-I debonding of a double cantilever beam: A comparison between cohesive crack modeling and Finite Fracture Mechanics, Int. J. Solids Struct. 124 (2017) 57–72, http://dx.doi.org/10.1016/j.ijsolstr.2017.06.007.
[45] V. Carollo, T. Guillén-Hernández, J. Reinoso, M. Paggi, Recent advancements on the phase field approach to brittle fracture for heterogeneous materials and structures, Adv. Model. Simul. Eng. Sci. 5 (1) (2018) 8, http://dx.doi.org/10.1186/s40323-018-0102-y.
[46] H. Henry, Limitations of the modelling of crack propagating through heterogeneous material using a phase field approach, Theor. Appl. Fract. Mech. 104 (2019) 102384, http://dx.doi.org/10.1016/j.tafmec.2019.102384.
[47] C. Kuhn, A. Schlüter, R. Müller, On degradation functions in phase field fracture models, Comput. Mater. Sci. 108 (2015) 374–384, http://dx.doi.org/10.1016/j.commatsci.2015.05.034.

[48] H. Amor, J.J. Marigo, C. Maurini, Regularized formulation of the variational brittle fracture with unilateral contact: Numerical experiments, J. Mech. Phys. Solids 57 (8) (2009) 1209–1229, http://dx.doi.org/10.1016/j.jmps.2009.04.011.
[49] C. Miehe, F. Welschinger, M. Hofacker, Thermodynamically consistent phase-field models of fracture: Variational principles and multi-field FE implementations, Internat. J. Numer. Methods Engrg. 83 (10) (2010) 1273–1311, http://dx.doi.org/10.1002/nme.2861.
[50] M. Strobl, T. Seelig, On constitutive assumptions in phase field approaches to brittle fracture, in: Procedia Structural Integrity, Vol. 2, Elsevier B.V., 2016, pp. 3705–3712, http://dx.doi.org/10.1016/j.prostr.2016.06.460.
[51] J. Storm, D. Supriatna, M. Kaliske, The concept of representative crack elements for phase-field fracture: Anisotropic elasticity and thermo-elasticity, Internat. J. Numer. Methods Engrg. 121 (5) (2020) 779–805, http://dx.doi.org/10.1002/nme.6244.
[52] J.W. Cahn, S.M. Allen, A Microscopic Theory for Domain Wall Motion and Its Experimental Verification in Fe-Al Alloy Domain Growth Kinetics, J. Phys. Colloques 38 (C7) (1977) C7–51–C7–54, http://dx.doi.org/10.1051/jphyscol:1977709.
[53] M. Wheeler, T. Wick, W. Wollner, An augmented-Lagrangian method for the phase-field approach for pressurized fractures, Comput. Methods Appl. Mech. Engrg. 271 (2014) 69–85, http://dx.doi.org/10.1016/j.cma.2013.12.005.
[54] T. Heister, M.F. Wheeler, T. Wick, A primal-dual active set method and predictor-corrector mesh adaptivity for computing fracture propagation using a phase-field approach, Comput. Methods Appl. Mech. Engrg. 290 (2015) 466–495, http://dx.doi.org/10.1016/j.cma.2015.03.009.
[55] K. Mang, T. Wick, W. Wollner, A phase-field model for fractures in nearly incompressible solids, Comput. Mech. 65 (1) (2020) 61–78.
[56] J. Wambacq, J. Ulloa, G. Lombaert, S. François, Interior-point methods for the phase-field approach to brittle and ductile fracture, Comput. Methods Appl. Mech. Engrg. 375 (2021) 113612, http://dx.doi.org/10.1016/j.cma.2020.113612.
[57] I. Steinbach, Phase-field models in materials science, Modelling Simulation Mater. Sci. Eng. 17 (7) (2009) 31, http://dx.doi.org/10.1088/0965-0393/17/7/073001.
[58] X. Li, J. Lowengrub, A. Rätz, Voigt, Solving PDEs in complex geometries: A diffuse domain approach, Commun. Math. Sci. 7 (1) (2009) 81.
[59] M. Plapp, Phase-Field Models, CISM Int. Cent. Mech. Sci., Courses Lect. 538 (2012) 129–175, http://dx.doi.org/10.1007/978-3-7091-1227-4_4.
[60] K. Ammar, B. Appolaire, G. Cailletaud, S. Forest, Combining phase field approach and homogenization methods for modelling phase transformation in elastoplastic media, Eur. J. Comput. Mech. 18 (5–6) (2009) 485–523, http://dx.doi.org/10.3166/ejcm.18.485-523.
[61] A. Durga, P. Wollants, N. Moelans, Evaluation of interfacial excess contributions in different phase-field models for elastically inhomogeneous systems, Modelling Simulation Mater. Sci. Eng. 21 (5) (2013) 55018, http://dx.doi.org/10.1088/0965-0393/21/5/055018.
[62] J. Mosler, O. Shchyglo, H. Montazer Hojjat, A novel homogenization method for phase field approaches based on partial rank-one relaxation, J. Mech. Phys. Solids 68 (1) (2014) 251–266, http://dx.doi.org/10.1016/j.jmps.2014.04.002.
[63] D. Schneider, E. Schoof, O. Tschukin, A. Reiter, C. Herrmann, F. Schwab, M. Selzer, B. Nestler, Small strain multiphase-field model accounting for configurational forces and mechanical jump conditions, Comput. Mech. 61 (3) (2018) 277–295, http://dx.doi.org/10.1007/s00466-017-1458-4.
[64] B. Svendsen, P. Shanthraj, D. Raabe, Finite-deformation phase-field chemomechanics for multiphase, multicomponent solids, J. Mech. Phys. Solids 112 (2018) 619–636, http://dx.doi.org/10.1016/j.jmps.2017.10.005.
[65] E. Tanné, T. Li, B. Bourdin, J.J. Marigo, C. Maurini, Crack nucleation in variational phase-field models of brittle fracture, J. Mech. Phys. Solids 110 (2018) 80–99, http://dx.doi.org/10.1016/j.jmps.2017.09.006.
[66] A. Kumar, B. Bourdin, G.A. Francfort, O. Lopez-Pamies, Revisiting nucleation in the phase-field approach to brittle fracture, J. Mech. Phys. Solids 142 (2020) 104027, http://dx.doi.org/10.1016/j.jmps.2020.104027.
[67] M. Klinsmann, D. Rosato, M. Kamlah, R.M. McMeeking, An assessment of the phase field formulation for crack growth, Comput. Methods Appl. Mech. Engrg. 294 (2015) 313–330, http://dx.doi.org/10.1016/j.cma.2015.06.009.
[68] K.H. Pham, K. Ravi-Chandar, C.M. Landis, Experimental validation of a phase-field model for fracture, Int. J. Fract. 205 (1) (2017) 83–101, http://dx.doi.org/10.1007/s10704-017-0185-3.
[69] X. Zhang, C. Vignes, S.W. Sloan, D. Sheng, Numerical evaluation of the phase-field model for brittle fracture with emphasis on the length scale, Comput. Mech. 59 (5) (2017) 737–752, http://dx.doi.org/10.1007/s00466-017-1373-8.
[70] K. Pham, J.-J. Marigo, The variational approach to damage: II. The gradient damage models, C. R. Méc. 338 (4) (2010) 199–206, http://dx.doi.org/10.1016/j.crme.2010.03.012.
[71] J.-Y. Wu, V.P. Nguyen, A length scale insensitive phase-field damage model for brittle fracture, J. Mech. Phys. Solids 119 (2018) 20–42, http://dx.doi.org/10.1016/j.jmps.2018.06.006.
[72] D. Arndt, W. Bangerth, B. Blais, T.C. Clevenger, M. Fehling, A.V. Grayver, T. Heister, L. Heltai, M. Kronbichler, M. Maier, P. Munch, J.P. Pelteret, R. Rastak, I. Tomas, B. Turcksin, Z. Wang, D. Wells, The deal.II library, Version 9.2, J. Numer. Math. 28 (3) (2020) 131–146, http://dx.doi.org/10.1515/jnma-2020-0043.
[73] A.C. Hansen-Dörr, J. Brummund, M. Kästner, Phase-field modeling of fracture in heterogeneous materials: jump conditions, convergence and crack propagation, Arch. Appl. Mech. 91 (2020) 1–18, http://dx.doi.org/10.1007/s00419-020-01759-3.
[74] A. Trauth, Characterisation and Modelling of Continuous-Discontinuous Sheet Moulding Compound Composites for Structural Applications, 2019, http://dx.doi.org/10.5445/IR/1000096578.
[75] J. Görthofer, N. Meyer, T.D. Pallicity, L. Schöttl, A. Trauth, M. Schemmann, M. Hohberg, P. Pinter, P. Elsner, F. Henning, A. Hrymak, T. Seelig, K. Weidenmann, L. Kärger, T. Böhlke, Virtual process chain of sheet molding compound: Development, validation and perspectives, Composites B 169 (2019) 133–147, http://dx.doi.org/10.1016/j.compositesb.2019.04.001.
[76] A. Trauth, M. Bondy, K.A. Weidenmann, W. Altenhof, Mechanical properties and damage evolution of a structural sheet molding compound based on a novel two step curing resin system, Mater. Des. 143 (2018) 224–237, http://dx.doi.org/10.1016/j.matdes.2018.02.002.

[77] C. Miehe, A. Koch, Computational micro-to-macro transitions of discretized microstructures undergoing small strains, Arch. Appl. Mech. 72 (4–5) (2002) 300–317, http://dx.doi.org/10.1007/s00419-002-0212-2.

[78] M. Schneider, The sequential addition and migration method to generate representative volume elements for the homogenization of short fiber reinforced plastics, Comput. Mech. 59 (2) (2017) 247–263, http://dx.doi.org/10.1007/s00466-016-1350-7.

[79] E. Schoof, C. Herrmann, N. Streichhan, M. Selzer, D. Schneider, B. Nestler, On the multiphase-field modeling of martensitic phase transformation in dual-phase steel using J_2-viscoplasticity, Modelling Simulation Mater. Sci. Eng. 27 (2) (2019) 025010, http://dx.doi.org/10.1088/1361-651X/aaf980.